Supporting Information for

Modulation of the Bonding between Copper and a Redox Active Ligand by Hydrogen Bonds and its Effect on Electronic Coupling and Spin States

Dolores L. Ross,[†] Andrew J. Jasniewski,[§] Joseph W. Ziller,[†] Emile L. Bominaar,*[⊥] Michael P. Hendrich,*[⊥] and A.S. Borovik*[†]

[†]Department of Chemistry, 1102 Natural Science II, University of California, Irvine, CA 92697
[§]Department of Molecular Biology and Biochemistry, University of California, Irvine, CA 92697
[⊥]Department of Chemistry, Carnegie Mellon University, Pittsburgh, PA 15213

Table of Contents

Experimental Section

Reagents and Materials. Unless otherwise stated, all manipulations were performed under nitrogen atmosphere in a Vacuum Atmospheres, Co. drybox. The metal precursor $Cu^{II}(OAc)_2 \bullet H_2O$ was obtained from Alfa Aesar and was used as received. The metal precursor $Cu^{II}(OAc)_2$ anhydrous was dried at 70 °C under vacuum for two days prior to use. The metathesis salt Bu_4NBr was obtained from Chem-Impex International, Inc. and dried at 70 °C under vacuum for two days prior to use. Reagents DBU and TBD were used as received. Potassium hydride (KH) as a 30% dispersion in mineral oil was filtered with a glass frit and washed with 20 mL pentane and Et_2O 5 times, dried under vacuum, and stored under an argon atmosphere. The ligand precursor H_3ibaps[1] and $[FeCp_2]BF_4$[2] were prepared according to literature procedures.

Physical Methods. Electronic absorption spectra for kinetics experiments were recorded in a 1 cm cuvette on an 8453E Agilent UV-vis spectrophotometer equipped with an Unisoku Unispeks cryostat. Room temperature electronic absorption spectra for determining extinction coefficients were recorded in a 1 cm cuvette on a Cary 50/60 spectrophotometer. ^{1}H nuclear magnetic resonance (NMR) spectra were collected using a Bruker CRYO500 spectrometer and referenced to the residual solvent peak. ATR-FTIR spectra were collected in the solid state using a Thermo Scientific Nicolet iS5 FT-IR spectrometer paired with an iD5 ATR accessory.

Electron paramagnetic resonance measurements. X-band and S-band EPR spectra were recorded on a Bruker spectrometer equipped with Oxford liquid helium cryostats. The quantification of all signals is relative to a CuEDTA spin standard. The concentration of the standard was derived from an atomic absorption standard (Aldrich). For all instruments, the microwave frequency was calibrated with a frequency counter and the magnetic field with a NMR gaussmeter. A modulation frequency of 100 kHz was used for all EPR spectra. The EPR simulation software (*SpinCount*) was written by one of the authors.[3]

Electrochemical Measurements. Cyclic voltammetry experiments were conducted using a CHI600C electrochemical analyzer under an N_2 atmosphere. A 2.0 mm glassy carbon electrode was used as the working electrode with a silver wire reference electrode and platinum wire counter electrode. A ferrocenium/ferrocene couple ($FeCp_2^+/FeCp_2$) was used to monitor the Ag wire reference electrode, and all potentials are referenced to the $[FeCp_2]^{+/0}$ couple. Elemental analyses were conducted on a PerkinElmer 2400 Series II CHNS elemental analyzer.

Molecular Structure Determination. For molecular structure determination (X-ray diffraction; XRD), Bruker SMART APEX II diffractometer was employed. Data collection and the unit-cell parameters determination was performed by APEX2 program package. The raw data was processed with SAINT and SADABS to get the reflection data file. The SHELXTL program was used for

subsequent calculations. The analytical scattering factors for neutral atoms were used throughout the analysis. Hydrogen atoms were included using a riding model.

X-ray Absorption Spectroscopy.

Cu K-edge X-ray absorption near edge structure (XANES) analysis was carried out on the ibaps-supported Cu complexes to assess the electronic properties of the metal center. In each sample, the XANES spectrum contains three features before the white line. The first is a pre-edge feature assigned to a 1s → 3d transition, followed by a 1s → 4p plus ligand-to-metal-charge-transfer (LMCT) "shakedown" transition, then a 1s → 4p 'main' transition.[3–5] The positions of these transitions are summarized in Table X1.

The position of the pre-edge feature has been shown to be indicative of a Cu(II) or Cu(III) site,[3–5] so the XANES analysis can be used to probe if an oxidation event occurs on the metal center. In our experiments, all of the ibaps-containing samples regardless of oxidizing equivalents used show a pre-edge feature centered at ~8979 eV, which falls in the range of Cu(II) centers. This energy also compares well to that for the copper starting material, $Cu(OAc)_2$ (8978.9 eV), and other Cu(II) species found in the literature.[4–9] The expected pre-edge energy for a Cu(III) site is ~8981 eV, which indicates that for 2-TBD and 2-OH_2, the oxidation event does not appear to be associated with the Cu center. Additionally, the 1s → 4p + LMCT shakedown is more prominent than the 1s → 4p main transition in the rising edge for each sample, although the line shapes and intensities are not identical between complexes. The positions of these features are also relatively invariant across the complexes studied, regardless of the number of oxidizing equivalents used. These results can collectively be interpreted as the series of Cu(ibaps) complexes being consistent with a Cu(II) assignment, with deviations in the spectral features due to ligand and geometric differences between complexes.

Preparative Methods.

$Bu_4N[Cu^{II}(ibaps)(OH_2)]$ (**1**-OH_2). **Method 1:** H_3ibaps (342 mg, 0.467 mmol) was dissolved in THF and KH (56.1 mg, 1.40 mmol) was added. The mixture was stirred for 1 hr, which was sufficient time for gas evolution to cease and the dark solution to take on a yellow tint. The solution

was treated with $Cu(OAc)_2 \bullet H_2O$ (93.2 mg, 0.467 mmol) followed by additional THF (2 mL) and stirred for 3 h to produce a heterogenous dark purple mixture. The reaction mixture was filtered to remove KOAc and then treated with Bu_4NBr (150.5 mg, 0.467mmol). After an additional two hours of stirring the reaction mixture was filtered to remove KBr, and the solvent was removed under reduced pressure yielding a dark purple powder (93 % yield). 96 % yield of KOAc and KBr was obtained.

Method 2: This method follows the same route until addition of metal salt beginning with H_3ibaps (284 mg, 0.388 mmol and KH, 46.6 mg, 1.16 mmol). $Cu(OAc)_2$ (72 mg, 0.39 mmol) was added and the reaction was stirred for 3 h at which time water (7 μL) was added. Following an additional hour of stirring the reaction was treated with Bu_4NBr (125 mg, 0.388 mmol). The reaction was stirred for another 1.5 h and then filtered to remove KBr and KOAc (94 % yield of solid byproduct) and the solvent was removed. Pink x-ray quality crystals were obtained through layering of pentane over a THF solution of crude product. (386 mg, 94 % crystalline yield) UV-vis: λ_{max}/nm (THF, ε, $M^{-1}cm^{-1}$): 420 (700), 490 (460), 540 (400), 650 (130), 990 (440); (DCM, ε, $M^{-1}\,cm^{-1}$): 480 (100), 565 (85), 965 (30), 660 (60); (1:1 DCM:THF, ε, $M^{-1}\,cm^{-1}$): 316 (24000), 341 (30000), 500 (360), 540 (330), 990 (260). EPR (X-band, ⊥, DCM:THF, 77 K): $g_1 = 2.03$ ($A_1 = -570$ MHz), $g_2 = 2.06$ ($A_2 = -50$ MHz), $g_3 = 2.03$ ($A_3 = -50$ MHz). Anal. Calcd (found) for $C_{58}H_{92}CuN_4O_5S_2$: C, 66.15 (66.53); H, 8.81 (9.00); N, 5.32 (5.27). FTIR (ATR, cm^{-1}): 3180 (br), 3050, 2960, 2925, 2864, 1600, 1565, 1560, 1460, 1440, 1420, 1380, 1360, 1312, 1298, 1286, 1270, 1258, 1245, 1230, 1208, 1193, 1165, 1151, 1130, 1120, 1101, 1064, 1058, 1035, 952, 940, 930, 900, 899, 882, 874, 841, 814, 759, 729, 725, 697, 653, 640, 633, 622, 614, 608, 603, 595, 588, 581, 578, 576, 569, 566, 560, 556, 553. ATR FTIR ν(OH)/(OD) = 3180; 2424 cm^{-1}, measured/calcd = 1.04.

General Procedures for Synthesis of $Bu_4N[Cu^{II}(ibaps)(L)]$ where L = DBU, TBD, TMG.

Method 1: $Bu_4N[Cu^{II}(ibaps)(OH_2)]$ was dissolved in THF giving a dark purple solution that was then treated with B and stirred for ~30 minutes. The solvent was then removed under reduced pressure yielding a purple residue which was triturated with pentane and dried.

Method 2: H_3ibaps was dissolved in THF and treated with 3 equiv of KH. Once gas evolution ceased, $Cu(OAc)_2$ was added, and the reaction was stirred for three hours. The base of choice was then added and after an additional 30 minutes Bu_4NBr was added. After 1.5 hours the reaction mixture was filtered to remove solid byproduct and the filtrate was pumped down to obtain powder of the product.

$Bu_4N[Cu^{II}(ibaps)(TBD)]$ (**1**-TBD). (80 % yield) UV-vis: λ_{max}/nm (THF, ε, $M^{-1}\,cm^{-1}$): 425 (1230), 540 (970), 1050 (430); (1:1 DCM:THF, ε, $M^{-1}\,cm^{-1}$): 316 (20000), 340 (25000), 430 (sh), 545 (900), 730 (680), 995 (390). EPR (X-band, ⊥, DCM:THF, 77 K): g_1 = 2.21 (A_1 = -375 MHz), g_2 = 2.05 (A_2 = 40 MHz), g_3 = 2.04 (A_3 = -175 MHz). Anal. Calcd (found) for $C_{65}H_{103}CuN_7O_4S_2 \cdot 1\ H_2O$: C, 65.48 (65.42); H, 8.88 (9.06); N, 8.22 (8.17). FTIR (ATR, cm^{-1}): 3300, 3042, 2956, 2932, 2864, 1616, 1606, 1558, 1552, 1475, 1465, 1437, 1421, 1379, 1360, 1321, 1315, 1275, 1238, 1230, 1192, 1163, 1124, 1061, 1059, 1036, 945, 894, 878, 842, 805, 725, 685, 648. ATR FTIR ν(OH)/(OD) = 3300; 2480 cm^{-1}, calc/obs = 0.97. CV (0.1 V/s): $E_{1/2}$ = -0.70 V vs. $[Fe^{III/II}Cp_2]^{+/0}$; i_a/i_c = 1.2, ΔE = 0.18; E_a' =+0.51 vs. $[Fe^{III/II}Cp_2]^{+/0}$.

$Bu_4N[Cu^{II}(ibaps)(TMG)]$ (**1**-TMG). The dark purple filtrate was concentrated under reduced pressure and layered under pentane at -30 °C giving pale purple solid (93 % yield). Anal. Calcd (found) for $C_{63}H_{103}CuN_7O_4S_2 \cdot 0.5$ pentane: C, 66.32 (66.38); H, 9.26 (9.44); N, 8.27 (8.11). λ_{max}/nm (1:1 DCM:THF, ε, $M^{-1}\,cm^{-1}$): 347 (29000), 340 (25000), 425 (2100), 525 (2100), 1000 (700). EPR (X-band, ⊥, DCM:THF, 77 K): g = 2.04, 2.06, 2.20 (A_z = 458 MHz). FTIR (ATR, cm^{-1}): 3330, 3043, 2956, 2932, 2867, 2794, 1600, 1565, 1555, 1529, 1477, 1462, 1435, 1426, 1414, 1380, 1358, 1307,

1278, 1267, 1237, 1195, 1162, 1126, 1107, 1058, 1037, 956, 945, 900, 895, 877, 842, 810, 760, 745, 723, 691, 654, 634, 622. ATR FTIR ν(OH)/(OD) = 3330; 2480 cm^{-1}, calc/obs = 0.98. CV (0.1 V/s): $E_{1/2}$ = -0.75 V vs. $[Fe^{III/II}Cp_2]^{+/0}$; i_a/i_c = 1.1, ΔE = 0.18; $E_{1/2}'$ =+0.60 vs. $[Fe^{III/II}Cp_2]^{+/0}$; i_a/i_c = 0.6, ΔE = 0.200 V.

$Bu_4N[Cu^{II}(ibaps)(DBU)]$ (**1**-DBU). The dark purple filtrate was concentrated under reduced pressure and layered under pentane at -30 °C giving dark purple crystals (91 % yield). λ_{max}/nm (1:1 DCM:THF, ε, M^{-1} cm^{-1}): 317 (23000, 340 (29000), 488 (500), 550 (600), 697 (320), 990 (300). EPR (X-band, ⊥, DCM:THF, 77 K): g = 2.03, 2.06, 2.21 (A_z = 419 MHz). FTIR (ATR, cm^{-1}): 3043, 2957, 2929, 2866, 1626, 1600, 1557, 1555, 1483, 1465, 1438, 1422, 1379, 1360, 1314, 1271, 1237, 1228, 1214, 1200, 1159, 1124, 1070, 1059, 1037, 946, 893, 878, 842, 795, 761, 748, 724, 680, 648, 630. CV (0.1 V/s): $E_{1/2}$ = -0.71 V vs. $[Fe^{III/II}Cp_2]^{+/0}$; i_a/i_c = 0.82, ΔE = 0.13; E_a' =+1.4 vs. $[Fe^{III/II}Cp_2]^{+/0}$.

General Procedure for Synthesis of the One-Electron Oxidized Species, [Cu(ibaps)(L)] where L = H_2O, DBU, TBD, TMG

$Bu_4N[Cu^{II}(ibaps)(L)]$ was dissolved in neat DCM giving a dark purple solution that immediately turned dark green upon addition of 1.1 equiv $FcBF_4$. The green filtrate was pumped down, washed with cold pentane, and dried giving the crude product.

[Cu(ibaps)(OH_2)] (**2**-OH_2). 87 % yield. UV-vis: λ_{max}/nm (THF, ε, M^{-1} cm^{-1}): 347 (20000), 380 (16000), 475 (4300), 530 (4000), 685 (5000), 970 (8000); (DCM, ε, M^{-1} cm^{-1}): 345 (20000), 375 (17000), 430 (4000), 547 (4000), 975 (8300); (1:1 DCM:THF, ε, M^{-1} cm^{-1}): 346 (20000), 380 (16000), 480 (2800), 532 (3300), 685 (3300), 965 (8400). EPR (X-band, ||, DCM:THF, 4 K): g = 4.1 (A = 195 MHz). Anal. Calcd (found) for $C_{42}H_{56}CuN_3O_5S_2$: C, 62.23 (62.24); H, 6.96 (7.12); N 5.18 (4.93). FTIR (ATR, cm^{-1}): 3225 (br), 3080, 3010, 2959, 2933, 2874, 1598, 1580, 1566, 1550, 1530, 1482,

1463, 1443, 1419, 1384, 1363, 1321, 1300, 1296, 1279, 1271, 1248, 1213, 1165, 1147, 1137, 1113, 1104, 1051, 1034, 940, 932, 927, 882, 844, 831, 822, 813, 757, 743, 740, 730, 706, 690, 678, 649, 624, 618, 614, 610, 604, 588, 584, 580, 575, 570, 566, 560, 558, 555. ATR FTIR ν(OH)/(OD) = 3225; 2424 cm^{-1}, measured/calcd = 0.97

[Cu(ibaps)(TBD)] (**2**-TBD). UV-vis: 47 % yield. λ_{max}/nm (THF, ε, $M^{-1}\,cm^{-1}$): 345 (16000), 380 (sh), 480 (5500), 505 (5400), 735 (9600), 915 nm (2800). λ_{max}/nm (1:1 DCM:THF, ε, $M^{-1}\,cm^{-1}$): 343 (21000), 472 (5200), 731(10000), 910sh (2700). ^{1}H NMR (500 MHz, CD_2Cl_2, rt, ppm): 0.90 (t 2H, solvent), (1.02 (t, 10H, Bu_4N (CH_3)), 1.15 (d, 16H, *o*-CH(C**H**$_3$)$_2$), 1.24 (d, 12H, *p*-CH(C**H**$_3$)$_2$), 1.45 (s, 7H, Bu_4N (CH_2)), 1.63 (s, 7H, Bu_4N (CH_2)), 1.88 (p, 2H, HTBD), 2.05 (p, 3H, HTBD), 2.89 (sept, 2H, *p*-C**H**(CH_3)$_2$), 3.16 (s, 6H, Bu_4N (CH_2)), 3.22 (q, 3H), 3.32 (t, 3H), 4.15 (s, 8H, ferrocene), 4.63 (s, 2H, OH), 4.77 (sept, 3H, *o*-C**H**(CH_3)$_2$), 6.96 (t, 2H, CH), 7.14-6 (m, 5H), 7.38 (m, 2H, CH), 7.82 (d, 2H, CH). Anal. Calcd (found) for $C_{49}H_{67}CuN_6O_4S_2$·1 THF: C, 63.41 (63.31); H, 7.53 (7.38); N, 8.37 (8.60). FTIR (ATR, cm^{-1}): 3330 (br), 3044, 2958, 2935, 2866, 1636, 1600, 1552, 1465, 1457, 1422, 1381, 1364, 1316, 1273, 1259, 1219, 1194, 1115, 1054, 1035, 939, 878, 842, 802, 749, 736, 652, 612, 588, 568. ATR FTIR ν(NH)/(ND) = 3330; 2480 cm^{-1}, measured/calcd = 0.98

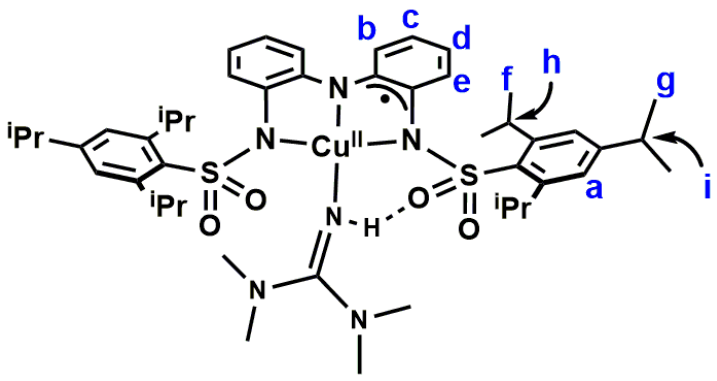

[Cu(ibaps)(TMG)] (**2**-TMG). 80 % yield. UV-vis: λ_{max}/nm (1:1 DCM:THF, ε, $M^{-1}\,cm^{-1}$): 342 (26000), 450 (6900), 665 (7100), 795 (8100), 920 (5600). ^{1}H NMR (500 MHz, CD_2Cl_2, rt, ppm): 1.02 (t, 15H, *o*-CH(C**H**$_3$)$_2$ – f, and Bu_4NBF_4 CH_3), 1.22 (d, 9H, *p*-CH(C**H**$_3$)$_2$ - g), 1.29 (m, 10H, *o*-CH(C**H**$_3$)$_2$ - f), 1.43 (sextet, 7H, Bu_4NBF_4 $NCH_2CH_2C\mathbf{H_2}CH_3$), 1.62 (pentet, 7H, Bu_4NBF_4 $NCH_2C\mathbf{H_2}CH_2CH_3$), 2.74 (s, 1H, HTMG or OH), 2.87 (pentet, 2H, *p*-C**H**(CH$_3$)$_2$ - i), 3.01 (s, 1H, HTMG or OH), 3.06 (s, 4H, HTMG), 3.15 (m, 6H, Bu_4NBF_4 $NC\mathbf{H_2}CH_2CH_2CH_3$), 3.34 (s, 4H, HTMG), 4.15 (s, 7H, Fc), 4.92 (septet, 4H, *o*-C**H**(CH$_3$)$_2$ - h), 6.06 (t, 2H, CH - d), 7.02 (d, 2H, CH - b), 7.15 (s, 4H, CH - a), 7.46 (t, 2H, CH - c), 7.51 (d, 2H, CH - e). FTIR (ATR, cm^{-1}): 3360, 3092, 3047, 2956, 2926, 2866, 2801, 1598, 1580, 1541, 1535, 1457, 1449, 1427, 1416, 1409, 1381, 1362, 1318, 1295, 1286, 1274, 1253, 1220, 1194, 1140, 1137, 1118, 1106, 1057, 1035, 1002, 933, 904, 882, 843, 816, 803, 752, 748, 732, 687, 650, 630, 615. ATR FTIR ν(NH)/(ND) = 3360; 2490 cm^{-1}, measured/calcd = 0.99

[Cu(ibaps)(DBU)] (**2**-DBU). 33 % yield. UV-vis: λ_{max}/nm (1:1 DCM:THF, ε, $M^{-1}\,cm^{-1}$): 341 (24000), 472 (6100), 718 (10600), 865 (5300). ^{1}H NMR (500 MHz, CD_2Cl_2, rt, ppm): 1.02 (t, 18H, *o*-CH(C**H**$_3$)$_2$ – f, and Bu_4NBF_4 CH_3), 1.22 (d, 18H, *p*-CH(C**H**$_3$)$_2$ - g), 1.42 (sextet, 10H, Bu_4NBF_4 $NCH_2CH_2C\mathbf{H_2}CH_3$), 1.63 (m, 13H, Bu_4NBF_4 $NCH_2C\mathbf{H_2}CH_2CH_3$), 1.76 (s, 4H), 2.00 (s, 2H, DBU), 2.20 (s, 2H, DBU), 2.84 (m, 4H), 3.15 (m, 8H, Bu_4NBF_4 $NC\mathbf{H_2}CH_2CH_2CH_3$), 3.42 (m, 8H, DBU), 3.90 (s, 2H), 4.15 (s, 9H, Fc), 4.86 (m, 3H, *o*-C**H**(CH$_3$)$_2$ - h), 5.07 (s, 2H), 5.26 (s, 1H), 7.17 (s, 3H,

CH - a), 7.31 (s, 1H, CH - a), 8.06 (t, 2H, CH - c or d), 8.17 (d, 2H, CH – b or e), 9.306 (s, 1H, CH aromatic), 9.63 (s, 1H, CH aromatic). FTIR (ATR, cm^{-1}): 2958, 2929, 2865, 1645, 1614, 1598, 1556, 1527, 1471, 1456, 1444, 1421, 1380, 1360, 1316, 1275, 1247, 1229, 1204, 1190, 1117, 1107, 1050, 1035, 1004, 982, 949, 931, 880, 843, 815, 800, 756, 738, 685, 650, 612.

Table S1. Crystallographic Information for **1**-OH_2, **1**-DBU, and **2**-TMG.

Complex	**1**-OH_2	**1**-DBU	**2**-TMG
Empirical Formula	$C_{58}H_{92}CuN_4O_5S_2$	$C_{67}H_{105}CuN_6O_4S_2$	$C_{47}H_{67}CuN_6O_4S_2$
Fw	1053.01	1186.22	907.72
T (K)	88(2)	100(2)	133(2)
Crystal system	Monoclinic	Monoclinic	Monoclinic
Space group	$P2_1/c$	C2/c	$P2_1/c$
a (Å)	10.1279(5)	29.0322(18)	8.9241(15)
b (Å)	20.5905(11)	20.3567(13)	34.561(6)
c (Å)	27.4740(14)	30.6773(18)	19.528(3)
α (°)	90	90	90
β (°)	93.0071(6)	118.050(2)	100.901(3)
γ (°)	90	90	90
V (Å^3)	5721.5(5)	16000.6(17)	5914.2(17)
Z	4	8	4
δcalcd (Mg/m^3)	1.222	0.985	1.019
GOF on F^2	1.033	2.248	1.076
R1 (all data, x Å)	(0.73 Å) 0.0377	(0.83 Å) 0.1862	(0.80 Å) 0.1625
wR2 (all data, x Å)	(0.73 Å) 0.1029	(0.83 Å) 0.5033	(0.80 Å) 0.2879

Table S2. Select distances (Å) or angles (°) for **1**-DBU and **2**-TMG.

Atoms	**1-DBU**	**2-TMG**
Cu1 – N1	1.889(6)	1.936(5)
Cu1 – N2	2.026(5)	1.988(6)
Cu1 – N3	2.041(5)	1.952(6)
Cu1 – N4	2.001(7)	1.916(6)
N2 ··· N3	3.967(7)	3.734(7)
N1 ··· O4	--	2.883(7)
N2 – Cu1 – N3	154.6(2)	142.8(2)
N1 – Cu1 – N4	159.3(3)	148.5(2)
τ_4-value	0.33	0.49

Table S3. Redox properties of **1**-L and relevant literature values.[a]

Complex	**Solvent**	$E_{1/2}$	$E_{1/2}$'
1-OH_2	DCM	−0.48	+0.44
	THF	[−0.54]	[+0.48]
1-TBD	DCM	−0.70	+0.51[b]
	THF	[−0.85]	[+0.39][b]
1-TMG	DCM	−0.75	+0.41
	THF	[−0.70]	[+0.68][b]
1-DBU	DCM	−0.71	+0.55[b]
	THF	[−0.87]	[+0.47]
[Cu(TD1•)(H_2O)][c]	MeCN	~ −0.6 (red)	−0.052
^{tBu}CuOH[d]	DMF	−1.05	−0.28

[a]V versus $[Fe^{III/II}Cp_2]^{+/0}$ observed at 100 mV/s where L = H_2O, TBD, DBU, or TMG; [b]E_{pa}, [c]ref 10; [d]ref 11.

Table S4. Electrochemical data (in eV) for **1-L** complexes from DFT and CV[a]

Ligand	$\Delta E_{1/2}$(L)	$\Delta E'_{1/2}$(L)	$E'_{1/2}$(L) – $E_{1/2}$(L)
		gas phase	
H_2O	0	0	3.47
TMG	–0.33	–0.37	3.43
TBD	–0.32	–0.40	3.39
DBU	–0.33	–0.34	3.47
		DCM	
H_2O	0	0	1.24 (0.92)
TMG	–0.26 (–0.27)	–0.23 (–0.03)	1.28 (1.16)
TBD	–0.27 (–0.22)	–0.21 (+0.07)	1.30 (1.21)
DBU	–0.27 (–0.23)	–0.17 (+0.11)	1.34 (1.26)

Table S5. XANES Measurements**.**

Compound	Pre-edge Energy (eV)
$[Cu^{II}OH_2]^-$	8979.20
$[Cu^{II}TBD]^-$	8979.21
$[CuOH_2]$	8979.21
[CuTBD]	8979.17

*Samples were prepared as 5 mM frozen solutions in THF.

Table S6. Δg_ξ dependent terms in eqs S3.1 and S3.2 for series **1-L**

L	g_x	g_y	g_z	$\frac{1}{3}(\Delta g_x + \Delta g_y + \Delta g_z)$	$-\frac{5}{42}(\Delta g_x + \Delta g_y) + \frac{2}{3}\Delta g_z$
H_2O	2.03	2.06	2.20	0.0967	0.1226
TBD	2.04	2.05	2.21	0.1000	0.1293
TMG	2.06	2.04	2.20	0.1000	0.1214
DBU	2.03	2.06	2.21	0.1000	0.1293

Table S7. Decomposition of experimental A tensor in **1-L** in isotropic and traceless components for all allowed sign combinations.

L	A_x	A_y	A_z	A^{iso}	A^{tl}_x	A^{tl}_y	A^{tl}_z	α^2	α'^2	$A^{SD,gs}_z$	$A^{SD,gs}_z$ (DFT)
H_2O	*-50*	*-50*	*-570*	*-223*	*173*	*173*	*-347*	*0.7442*	*0.8213*	*-469*	-457
	-50	50	-570	-190	140	240	-380	0.6667	0.8796	-503	
	50	-50	-570	-190	240	140	-380	0.6268	0.8796	-503	
	50	50	-570	-157	207	207	-413	0.5891	0.9379	-536	
TBD	-175	-40	-375	-197	22	157	-178	0.6899	0.5383	-308	
	-175	*40*	*-375*	*-170*	*-5*	*210*	*-205*	*0.6279*	*0.5850*	*-334*	-349
	175	-40	-375	-80	255	40	-295	0.4186	0.7425	-424	
	175	40	-375	-53	228	93	-322	0.3566	0.7892	-451	
TMG	*-20*	*-10*	*-460*	*-163*	*143*	*153*	*-297*	*0.6124*	*0.7317*	*-418*	-385
	-20	10	-460	-157	137	167	-303	0.5969	0.7433	-425	
	20	-10	-460	-150	170	140	-310	0.5814	0.7550	-431	
	20	10	-460	-143	163	153	-317	0.5659	0.7667	-438	
DBU	-110	-55	-420	-195	85	140	-225	0.6860	0.6200	-354	
	-110	*55*	*-420*	*-158*	*48*	*213*	*-262*	*0.6008*	*0.6842*	*-391*	-351
	110	-55	-420	-122	232	67	-298	0.5155	0.7483	-428	
	110	55	-420	-85	195	140	-335	0.4302	0.8125	-464	

Table S8. Selected solutions from Table S7 based on trend and agreement with DFT.

L	α^2	α'^2	A^{iso}	A^{tl}_x	A^{tl}_y	A^{tl}_z	$A^{SD,gs}_z$	A^{SD}_z (DFT)
H_2O	0.6866	0.8208	-205	165	200	-365	-492	-457
TBD	0.5759	0.6096	-155	10	220	-230	-366	-349
TMG	0.5948	0.7029	-167	136	157	-293	-422	-385
DBU	0.6008	0.6842	-158	48	213	-262	-391	-351

Table S9. DFT (b3lyp/tzvp) Mulliken spin populations (SP) at selected atoms for the broken symmetry (BS) and ferromagnetic (F) spin states of **2**-H_2O and **2**-DBU[a]

Number [b]	Element	**2**-H_2O		**2**-DBU	
		BS	F	BS	F
1	Cu	0.571	0.570	0.413	0.561
2	N	-0.210	0.505	-0.160	0.485
3	N	0.049	0.145	0.008	0.148
4	N	0.025	0.143	0.037	0.150
5	C	0.047	-0.058	0.024	-0.055
6	C	-0.096	0.108	-0.067	0.105
7	C	0.033	-0.036	0.011	-0.034
8	C	-0.152	0.157	-0.114	0.153
9	C	0.072	-0.070	0.047	-0.067
10	C	-0.141	0.150	-0.113	0.145
11	C	0.045	-0.059	0.047	-0.055
12	C	-0.104	0.116	-0.069	0.116
13	C	0.034	-0.038	0.030	-0.037
14	C	-0.171	0.174	-0.100	0.164
15	C	0.085	-0.084	0.054	-0.073
16	C	-0.161	0.171	-0.102	0.153
17	O or N	0.061	0.058	0.057	0.094

[a]Notice that the SPs for the BS ground state of **2**-DBU are systematically lower in magnitude than in the other three columns, consistent with the model of Figure 10. [b]Atom numbers defined in the structure are below.

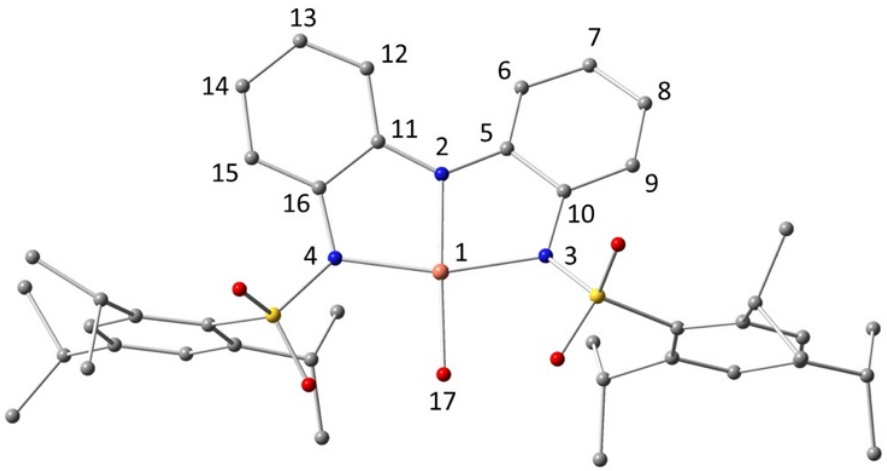

Table S10. Selected ligand bond distances (Å) for **1**-X, **2**-X (X = OH_2, DBU) and their respective changes from DFT (b3lyp/tzvp).[a]

Bond	**n**-H_2O			**n**-DBU		
	n = 1	**n** = 2, F[b]	$\Delta R_{ox\text{-}red}$	**n** = 1	**n** = 2, BS[b]	$\Delta R_{ox\text{-}red}$
Cu1-N2	1.915	1.945	0.030	1.966	2.027	0.061
Cu1-N3	2.030	2.029	-0.001	2.108	2.073	-0.035
Cu1-N4	2.045	2.036	-0.009	2.114	2.060	-0.054
Cu1-O17/N17	2.019	1.973	-0.046	2.043	2.009	-0.034
N2-C5	1.385	1.366	-0.019	1.366	1.343	-0.023
N2-C11	1.379	1.361	-0.018	1.380	1.367	-0.013
N3-C10	1.415	1.385	-0.030	1.400	1.357	-0.043
N4-C16	1.413	1.384	-0.029	1.400	1.372	-0.028
C5-C6	1.404	1.413	0.009	1.409	1.422	0.013
C6-C7	1.392	1.378	-0.014	1.388	1.371	-0.017
C7-C8	1.387	1.401	0.014	1.391	1.411	0.020
C8-C9	1.394	1.383	-0.011	1.392	1.374	-0.018
C9-C10	1.394	1.404	0.010	1.400	1.418	0.018
C5-C10	1.430	1.441	0.011	1.441	1.459	0.018
C11-C12	1.405	1.415	0.010	1.405	1.413	0.008
C12-C13	1.391	1.376	-0.015	1.392	1.379	-0.013
C13-C14	1.386	1.401	0.015	1.388	1.401	0.013
C14-C15	1.395	1.383	-0.012	1.394	1.380	-0.014
C15-C16	1.394	1.405	0.011	1.398	1.410	0.012
C11-C16	1.435	1.445	0.011	1.437	1.447	0.010

[a] Atom numbers defined in the diagram are below Table S9. [b] Data for ground state.

Table S11. DFT-calculated L-Cu-N1 bond angles for **3**-L and [Cu(ibaps^{T})L]$^{+}$ complexes.[a]

Complex	**3**-L (deg)
[Cu(ibaps)OH_2]$^{+}$	172
[Cu(ibaps^{T})OH_2]$^{+}$	176
[Cu(ibaps)TMG]$^{+}$	158
[Cu(ibaps)DBU]$^{+}$	149
[Cu(ibaps^{T})DBU]$^{+}$	179
[Cu(ibaps)TBD]$^{+}$	152
[Cu(ibaps^{T})TBD]$^{+}$	179
[Cu(ibaps^{T})N(H)CH_2]$^{+}$	178
[Cu(ibaps^{T})NH_3]$^{+}$	175

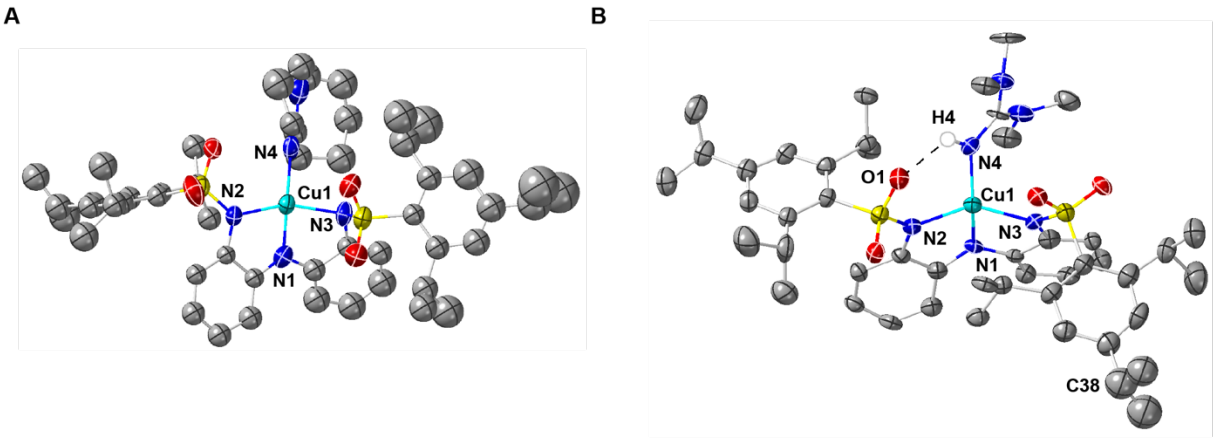

Figure S1. Thermal ellipsoid plots of **1**-DBU (**A**) and **2**-TMG (**B**). The counterion and hydrogen atoms are removed for clarity, except the one in **2**-TMG that H-bonds. Only one of the disordered isopropyl groups containing C38 is displayed. The C-atoms are represented as isotropic ellipsoids in **A**.

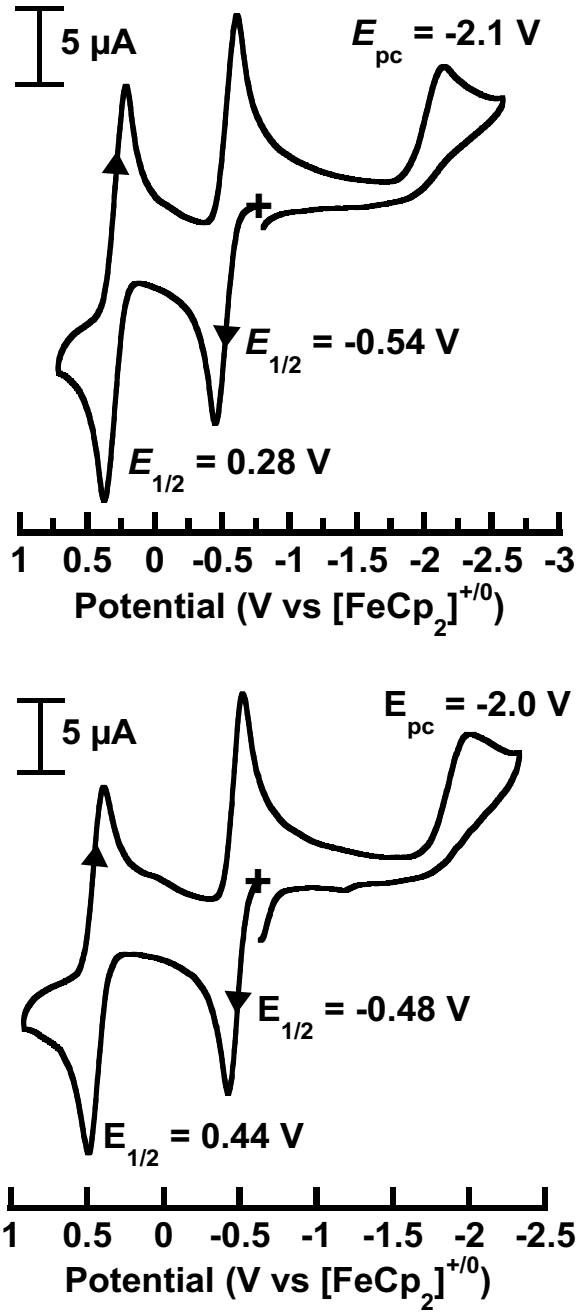

Figure S2. Cyclic voltammograms of **1**-OH_2. Conditions: 1 mM in THF (left) or DCM (right) with glassy carbon working electrode, platinum counter electrode, silver wire reference electrode and $TBAPF_6$ as the electrolyte. Ferrocene was used as the internal standard.

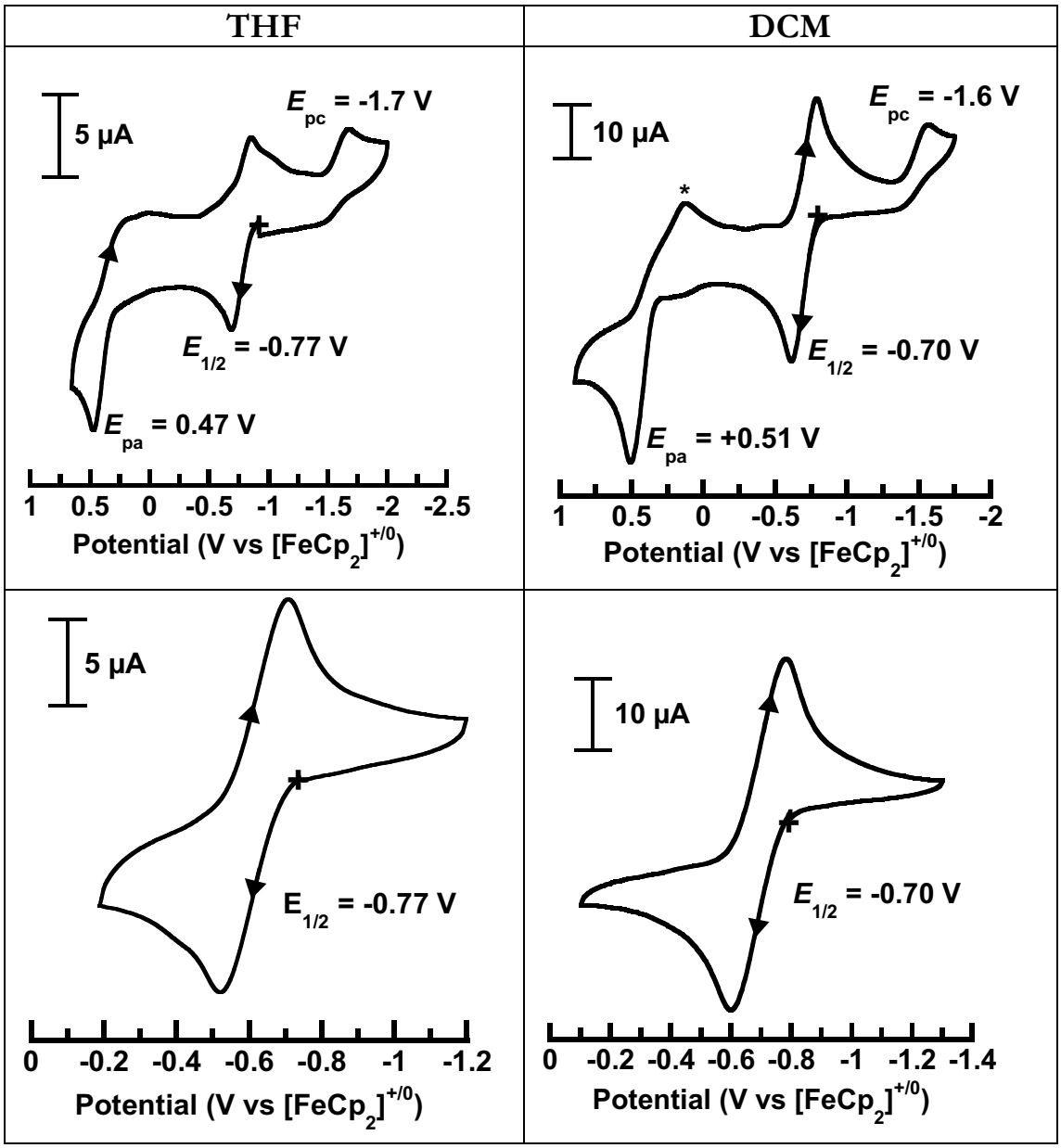

Figure S3. Cyclic voltammograms of **1**-TBD. CVs were collected in THF (left) and DCM (right). All features are shown in the top panels and the first oxidation events are shown in the bottom panels. Conditions: 1 mM in THF (left) or 2 mM in DCM (right) with glassy carbon working electrode, platinum counter electrode, silver wire reference electrode and $TBAPF_6$ as the electrolyte. Ferrocene was used as the internal standard.

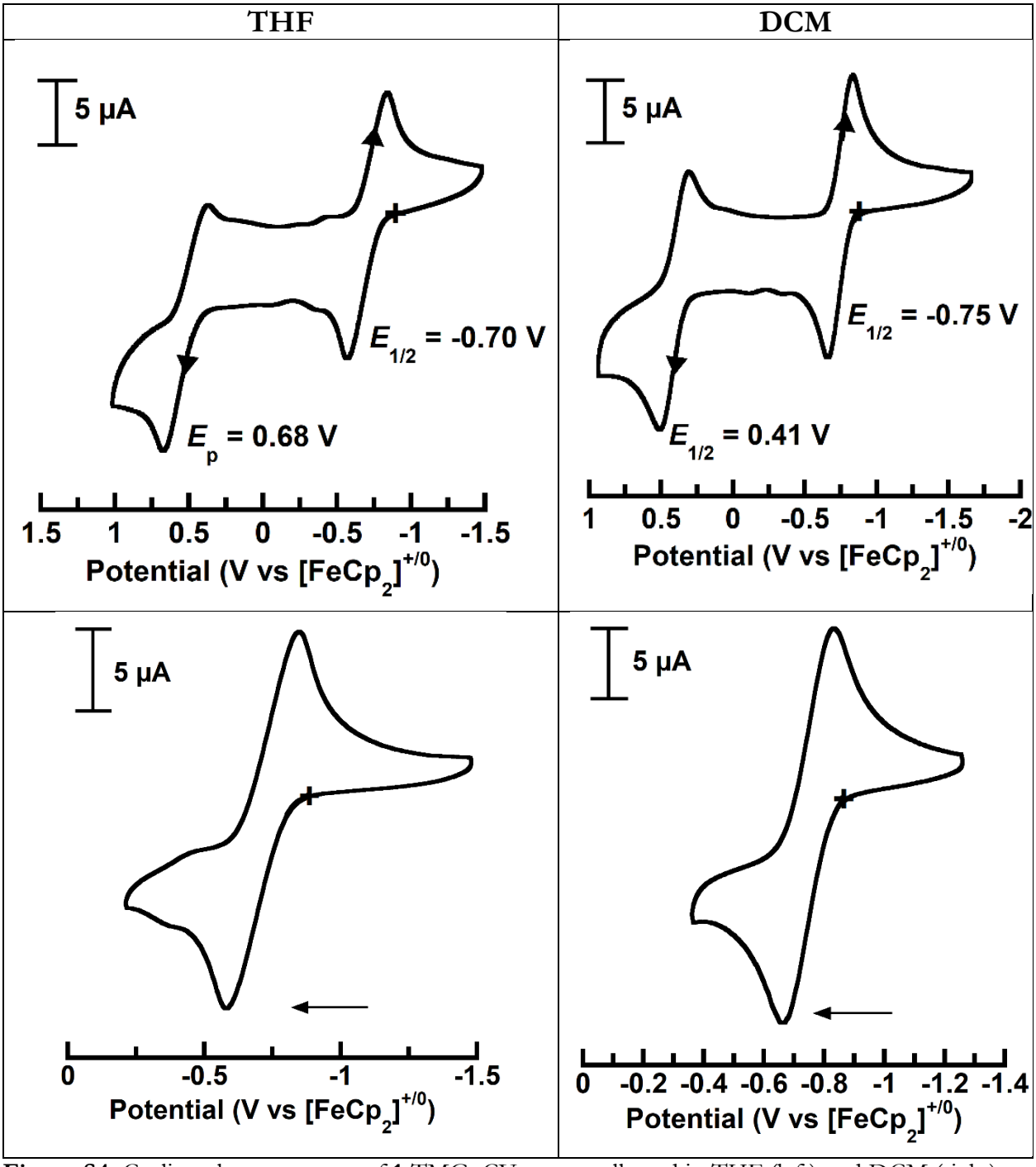

Figure S4. Cyclic voltammograms of **1**-TMG. CVs were collected in THF (left) and DCM (right). All features are shown in the top panels and the first oxidation events are shown in the bottom panels. Conditions: 1 mM in THF (left) or 1 mM in DCM (right) with glassy carbon working electrode, platinum counter electrode, silver wire reference electrode and $TBAPF_6$ as the electrolyte. Cobaltocenium was used as the internal standard.

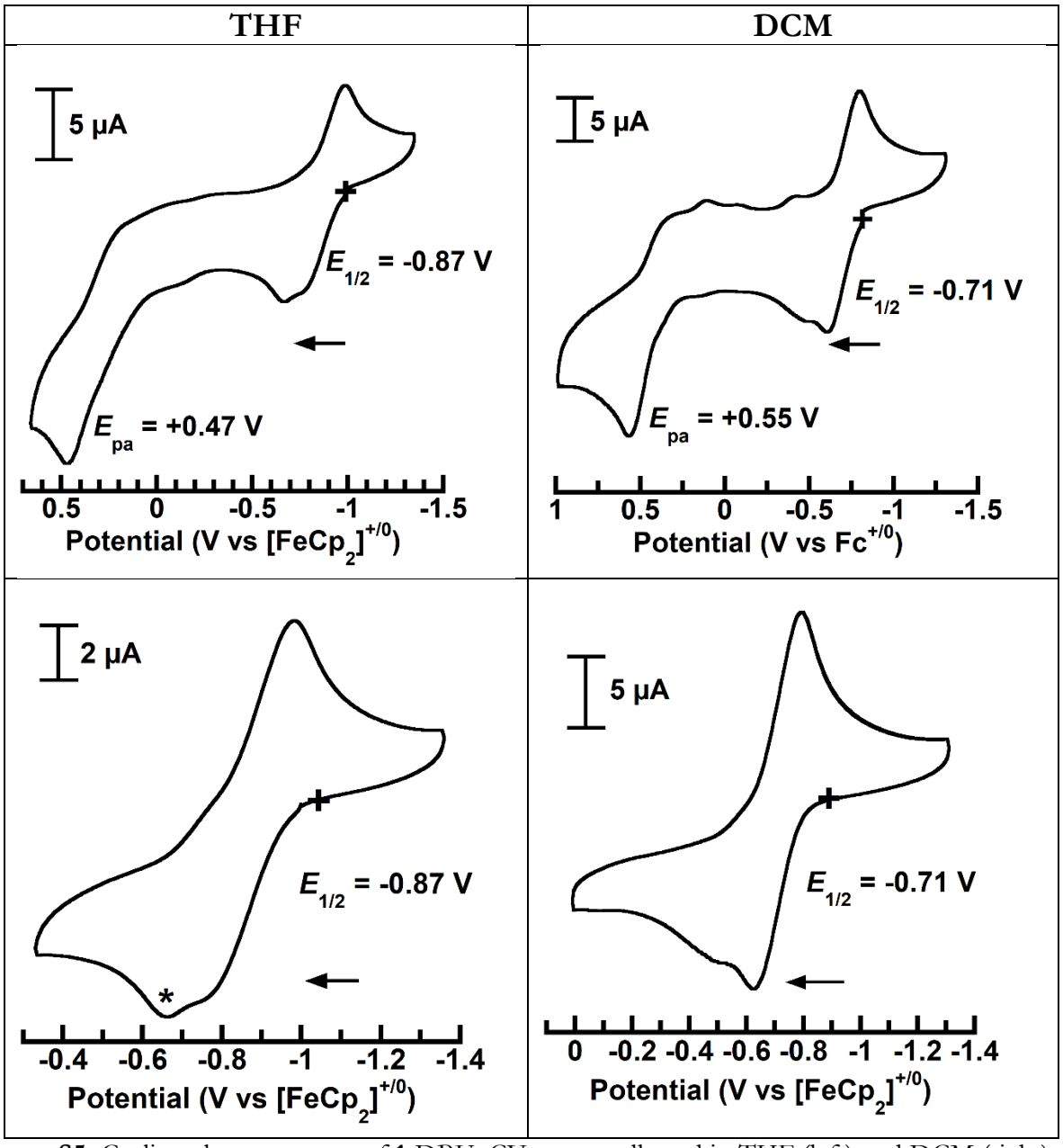

Figure S5. Cyclic voltammograms of **1**-DBU. CVs were collected in THF (left) and DCM (right). All features are shown in the top panels and the first oxidation events are shown in the bottom panels. Conditions: 1 mM in THF (left) or 1 mM in DCM (right) with glassy carbon working electrode, platinum counter electrode, silver wire reference electrode and $TBAPF_6$ as the electrolyte. Cobaltocenium was used as the internal standard.

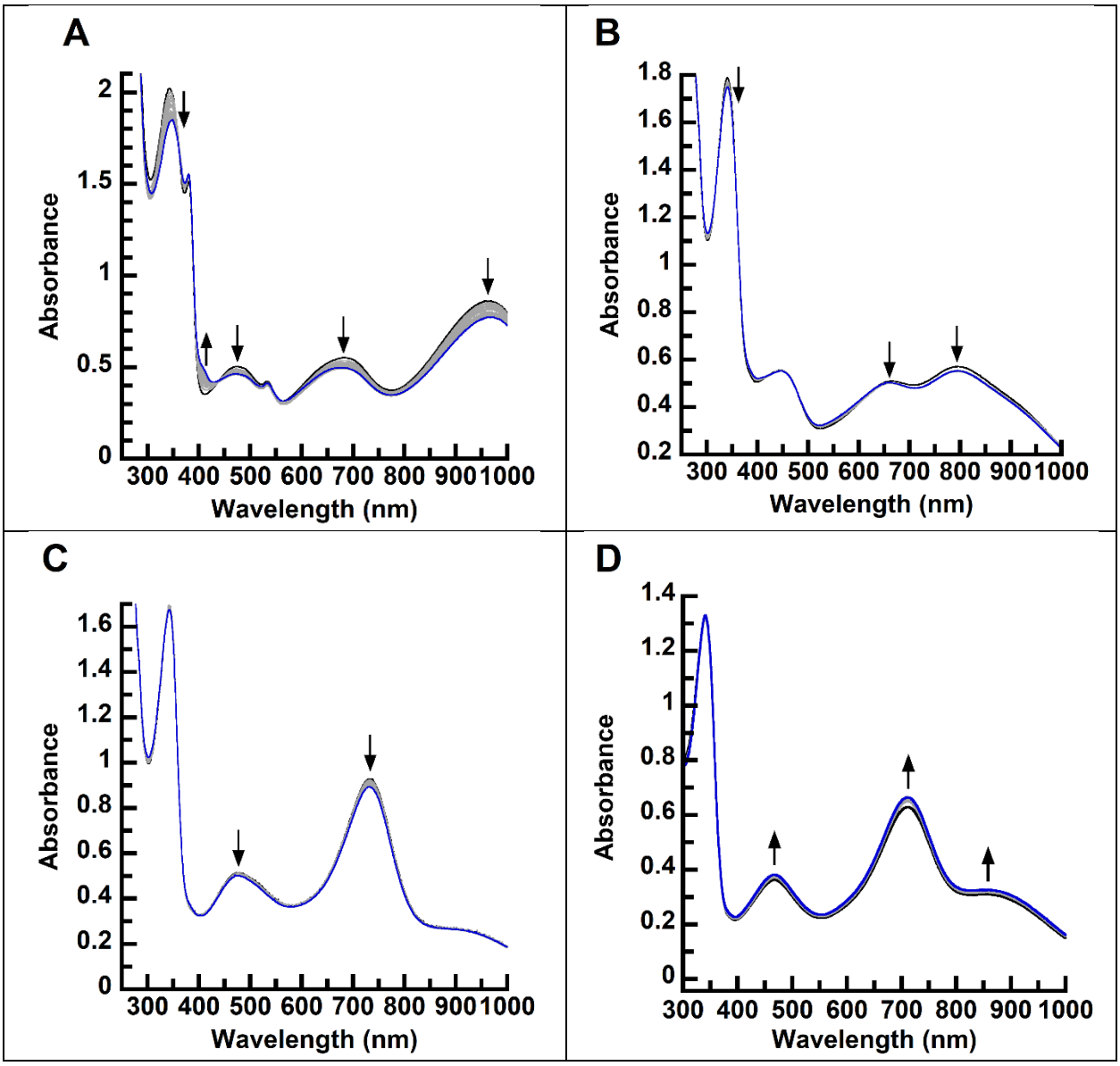

Figure S6. Electronic absorbance spectra of **2**-L to monitor stability. Complexes were dissolved as DCM:THF solutions at 22 °C with scans collected every hour for 20 hours. The initial spectrum is shown in black and the final is shown in blue. (A) **2**-OH_2 (0.1 mM), (B) **2**-TMG (0.1 mM), (C) **2**-TBD (0.1 mM), (D) **2**-DBU (0.05 mM).

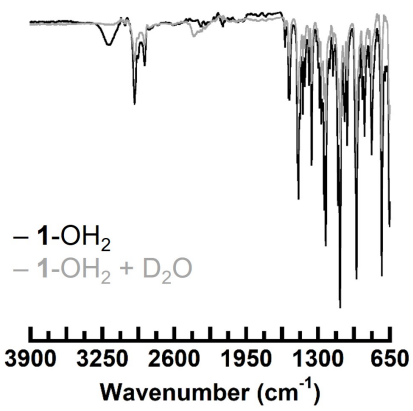
– 1-OH2
– 1-OH2 + D2O
3900 3250 2600 1950 1300 650
Wavenumber (cm-1)

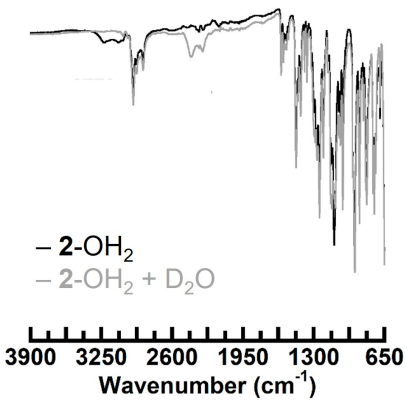
– 2-OH2
– 2-OH2 + D2O
3900 3250 2600 1950 1300 650
Wavenumber (cm-1)

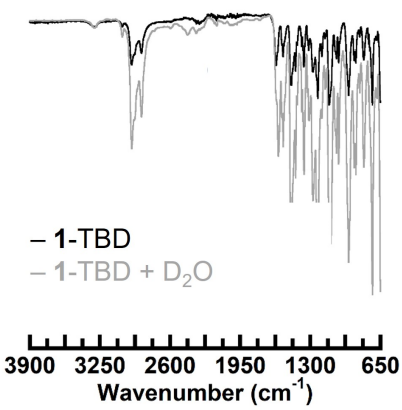
– 1-TBD
– 1-TBD + D2O
3900 3250 2600 1950 1300 650
Wavenumber (cm-1)

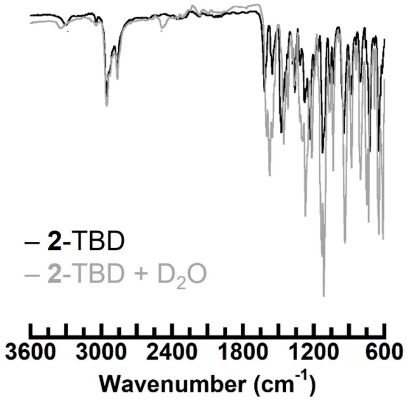
– 2-TBD
– 2-TBD + D2O
3600 3000 2400 1800 1200 600
Wavenumber (cm-1)

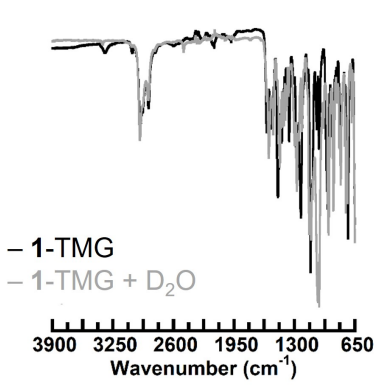
– 1-TMG
– 1-TMG + D2O
3900 3250 2600 1950 1300 650
Wavenumber (cm-1)

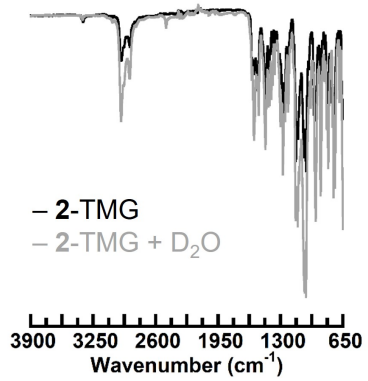
– 2-TMG
– 2-TMG + D2O
3900 3250 2600 1950 1300 650
Wavenumber (cm-1)

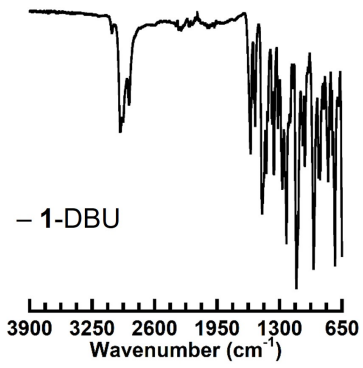
– 1-DBU
3900 3250 2600 1950 1300 650
Wavenumber (cm-1)

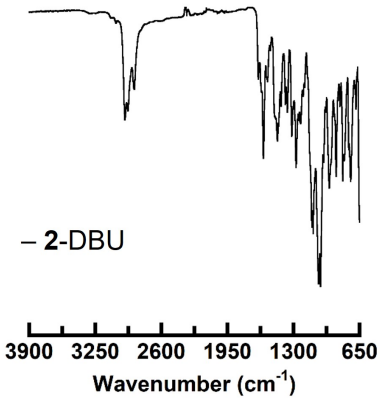
– 2-DBU
3900 3250 2600 1950 1300 650
Wavenumber (cm-1)

Figure S7. ATR FTIR spectra. Spectra of **1**-L and **2**-L (black) and their deuterated analogues (gray) in the solid state.

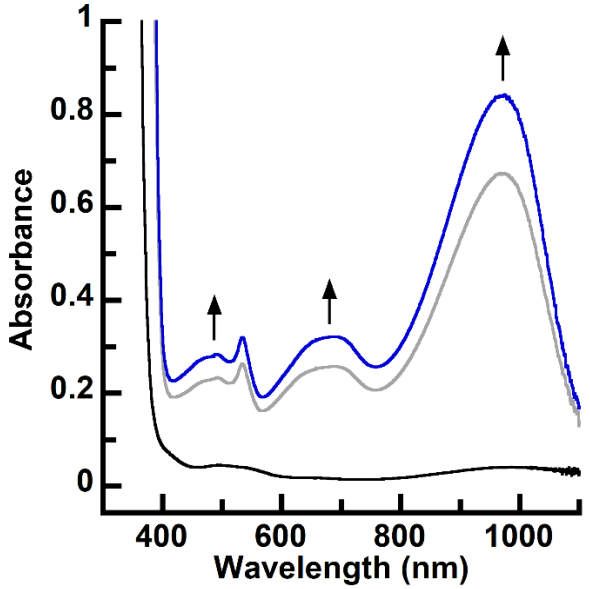

Figure S8. Oxidation of **1**-OH_2 monitored by UV-vis spectroscopy. Addition of 1.1 equiv of $[FeCp_2]BF_4$ (11 μL of 20 mM solution in DCM) to **1**-OH_2 (black) as a 0.1 mM solution in 1:1 DCM:THF. Each spectrum was collected in 1 s intervals. The intermediate scans are shown in gray and the product of the reaction (**2**-OH_2) is the blue trace. Experimental conditions: 1 cm cuvette, room temperature, under N_2.

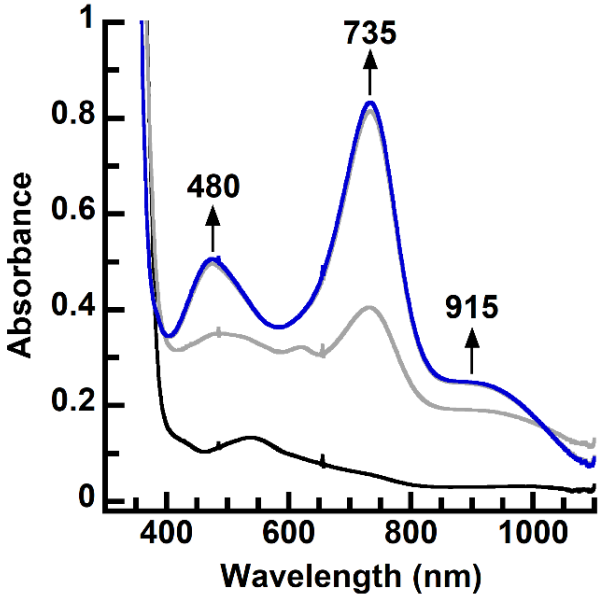

Figure S9. Generation of **2**-TBD via UV-vis spectroscopy from **1**-TBD. Electronic absorbance spectrum of **1**-TBD (black) + 1.4 equiv of $[FeCp_2]BF_4$ to give **2**-TBD (blue). Experimental

conditions: room temperature, [initial] 0.1 mM THF, intermediate scans shown in gray were collected every 1 s.

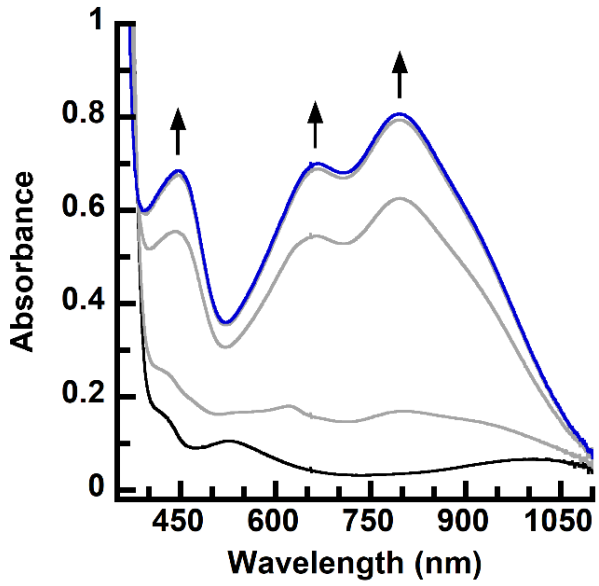

Figure S10. Generation of **2**-TMG via UV-vis spectroscopy from **1**-TMG. **1**-TMG (black) as a 0.1 mM DCM:THF solution was treated with 1 equiv of $FcBF_4$ (10 μL of a 20 mM DCM solution) generating **2**-TMG (blue). Intermediate time traces in gray were collected every 1 s and the reaction was complete after 5 s.

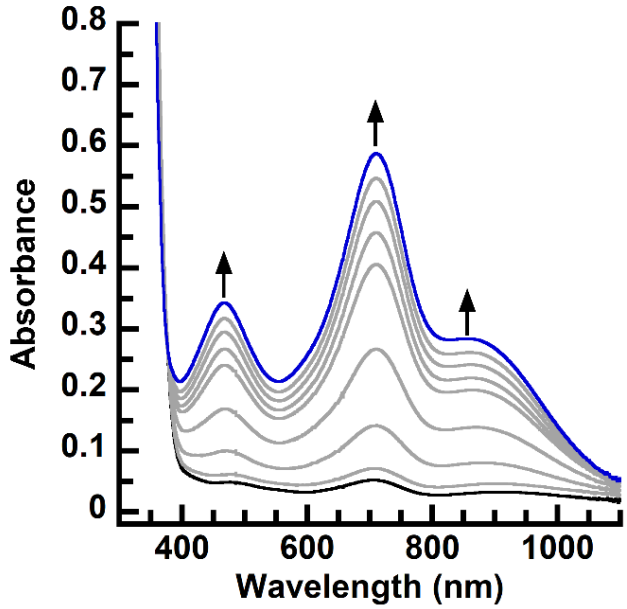

Figure S11. Generation of **2**-DBU via UV-vis spectroscopy from **1**-DBU. **1**-DBU (black) as a 0.05 mM DCM:THF solution was treated with 1 equiv of $FcBF_4$ (10 μL of a 10 mM DCM solution) generating **2**-DBU (blue).

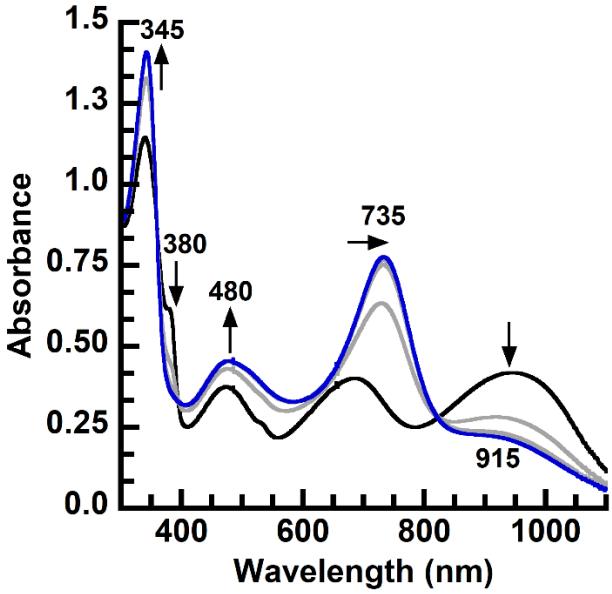

Figure S12. Generation of **2**-TBD via UV-vis spectroscopy from **1**-OH_2. Electronic absorbance spectrum of **2**-OH_2 (black) + 1 equiv TBD to give **2**-TBD (blue). Experimental conditions: room temperature, [initial] 0.1 mM THF, intermediate scans shown in gray were collected every 5 s.

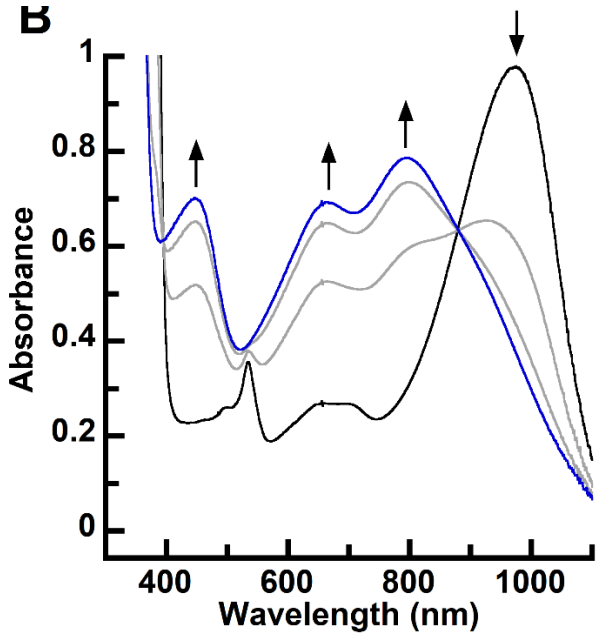

Figure S13. Generation of **2**-TMG via UV-vis spectroscopy from **2**-OH_2. **2**-OH_2 (black) as a 0.1 mM DCM:THF solution was treated with 1 equiv of TMG (10 μL of a 20 mM DCM:THF), followed by two portions of 0.5 equiv generating **2**-TMG (blue).

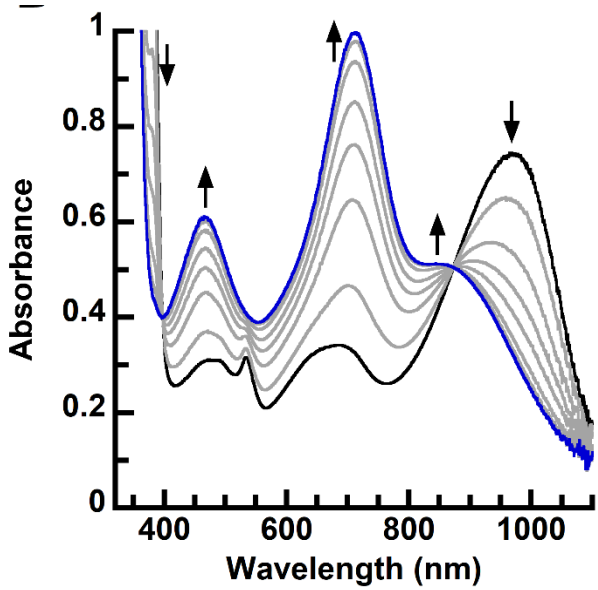

Figure S14. Generation of **2**-DBU via UV-vis spectroscopy from **2**-OH_2. **2**-OH_2 (black) as a 0.1 mM DCM:THF solution was treated with 1 equiv of DBU (10 μL of a 20 mM DCM:THF) generating **2**-DBU (blue). Intermediate time traces were collected every 0.5 seconds.

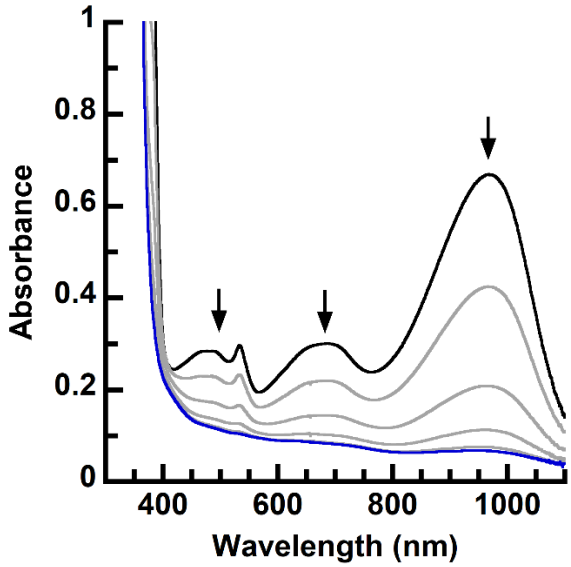

Figure S15. Reduction of **2**-OH_2 monitored by UV-vis spectroscopy. A 0.1 mM solution of **1**-OH_2 in DCM:THF was treated with 1 equiv of $[FeCp_2]BF_4$ (10 μL of a 10 mM DCM solution) to generate **2**-OH_2 in situ (black). The reaction mixture was then treated with 1.5 equiv of $CoCp_2$ (15 μL of a 10 mM DCM solution). Intermediate scans collected every 0.5 s are shown in gray and the final spectrum which was collected after 6 s is shown in blue. Experimental conditions: 22 °C.

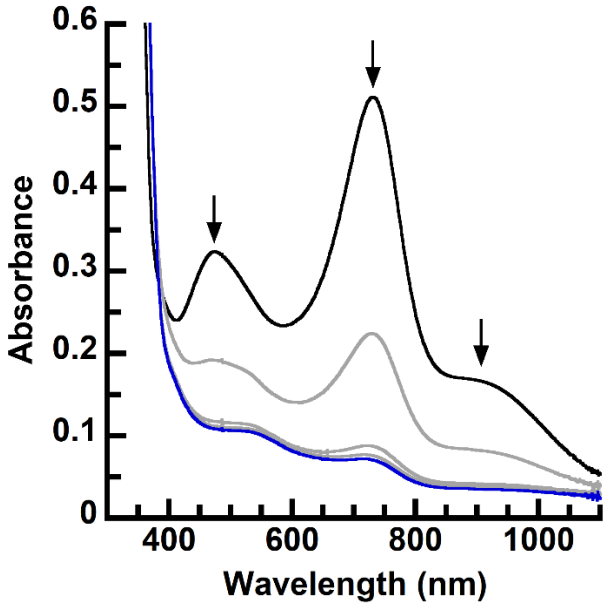

Figure S16. Reduction of **2**-TBD monitored by UV-vis spectroscopy. **1**-TBD was prepared as a 0.05 mM in DCM:THF and oxidized in situ with 1 equiv of $[FeCp_2]BF_4$ (10 μL of a 10 mM DCM solution) giving **2**-TBD (black trace). The reaction mixture was treated with 1.5 equiv of $CoCp_2$ (23 μL of a 6.7 mM DCM solution). The gray traces are intermediate scans collected every 1 s. The final spectrum collected after 5 seconds, is shown in blue.

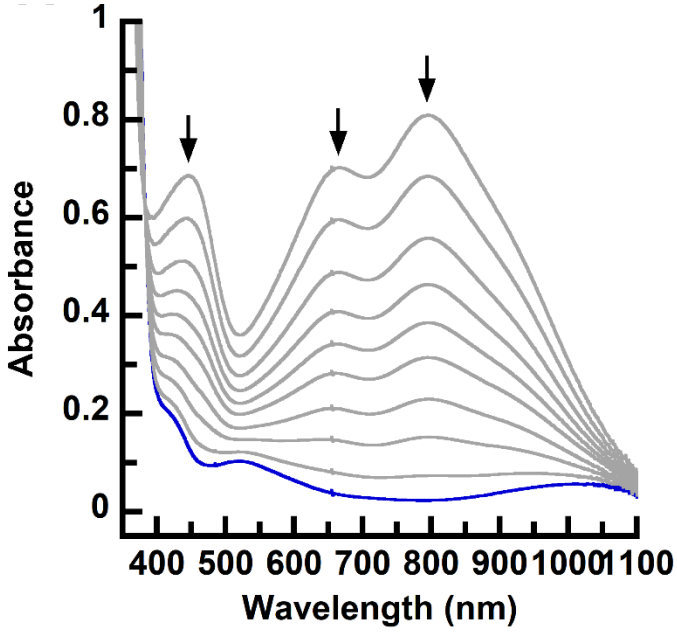

Figure S17. Reduction of **2**-TMG monitored by UV-vis spectroscopy. **1**-TMG in a 0.1 mM DCM:THF solution was treated with 1 equiv of $FcBF_4$ (10 μL of a 20 mM DCM solution) generating **2**-TMG which was treated with 2 equiv of $CoCp_2$ resulting in regeneration of **1**-TMG (blue). Gray traces were collected every 25 s and the reaction was completed after 4.5 minutes.

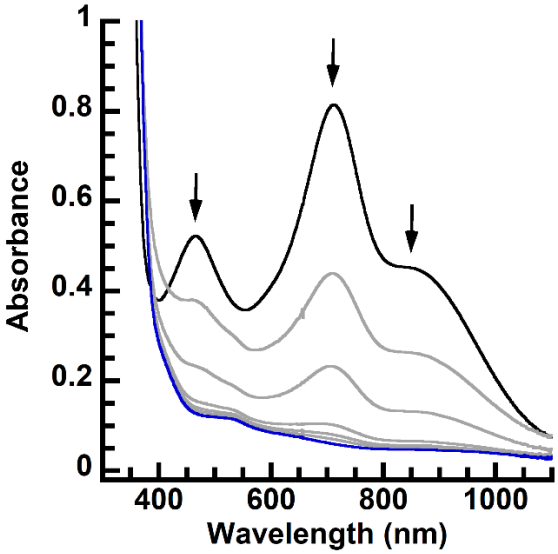

Figure S18. Reduction of **2**-DBU monitored by UV-vis spectroscopy.

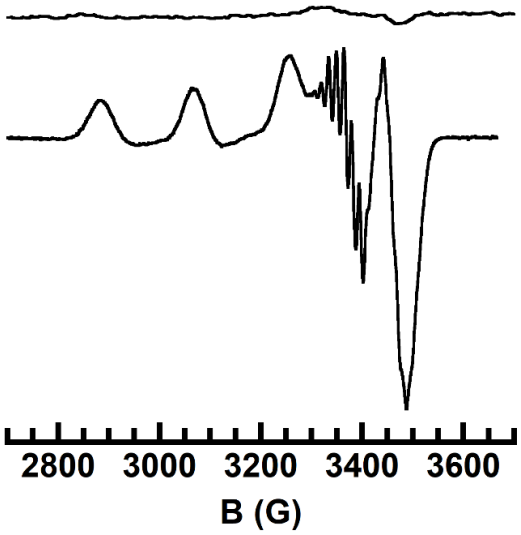

Figure S19. Reduction of **2**-OH_2 monitored by EPR spectroscopy. A 3.2 mM purple solution of **2**-OH_2 was prepared in THF and an EPR spectrum was obtained which revealed the silent spectrum (top). The sample was thawed and treated with 1 equiv of $CoCp_2$ (36 μL of a 20 mM solution in THF). The mixture was allowed to react for 2.5 minutes prior to freezing during which time the color changed to pale orange/gold. An EPR spectrum of the reaction mixture (2.75 mM Cu^{II}) was obtained (bottom). Experimental conditions: ⊥-mode EPR spectroscopy, 77 K, 9.62 GHz.

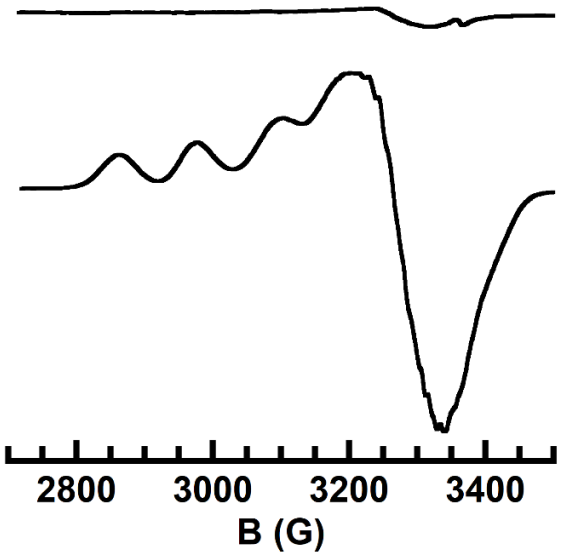

Figure S20. Reduction of **2**-TBD monitored by EPR spectroscopy. A purple 3 mM solution of **1**-TBD was prepared in a 1:1 DCM:THF mixture. A 200 μL sample was treated with 1.05 equiv (32 μL) of a 20 mM $[FeCp_2]BF_4$ solution in DCM causing the color to darken and giving the silent spectrum (top). The sample was thawed at –40 °C and treated with 1.1 equiv (20 μL) of a 50 mM $CoCp_2$ solution in DCM:THF causing a color change to orange/pink. The resulting EPR spectrum was obtained (bottom).

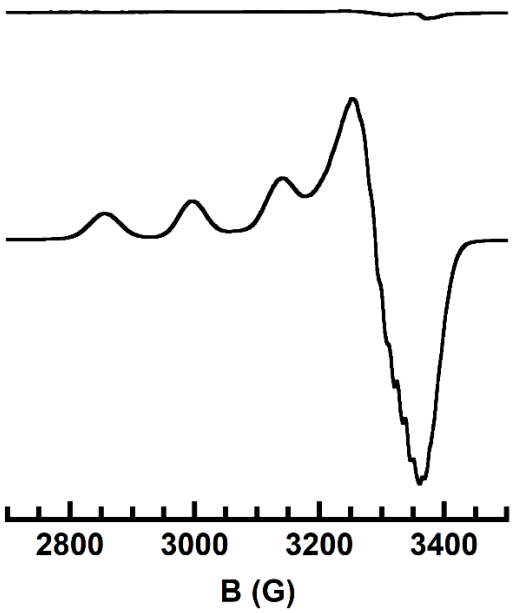

Figure S21. Reduction of **2**-TMG monitored by EPR spectroscopy. **2**-TMG (top) in DCM:THF was treated with 1.1 equiv of $CoCp_2$ as a DCM:THF solution giving the bottom spectrum.

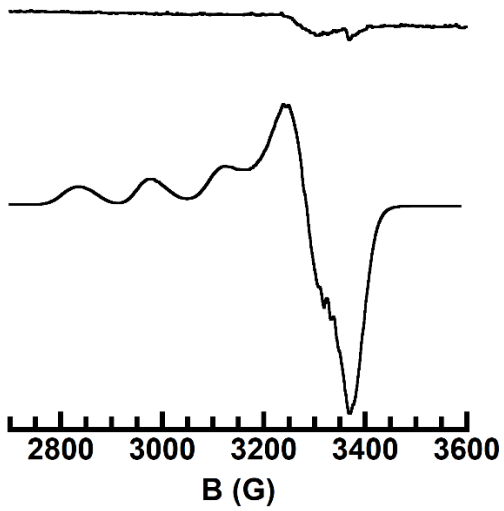

Figure S22. Reduction of **2**-DBU monitored by EPR spectroscopy.

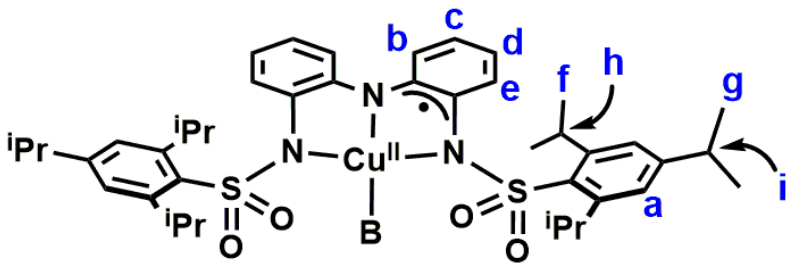

Figure S23. Labeling scheme for NMR spectra for **2**-X where X = TBD, TMG, and DBU.

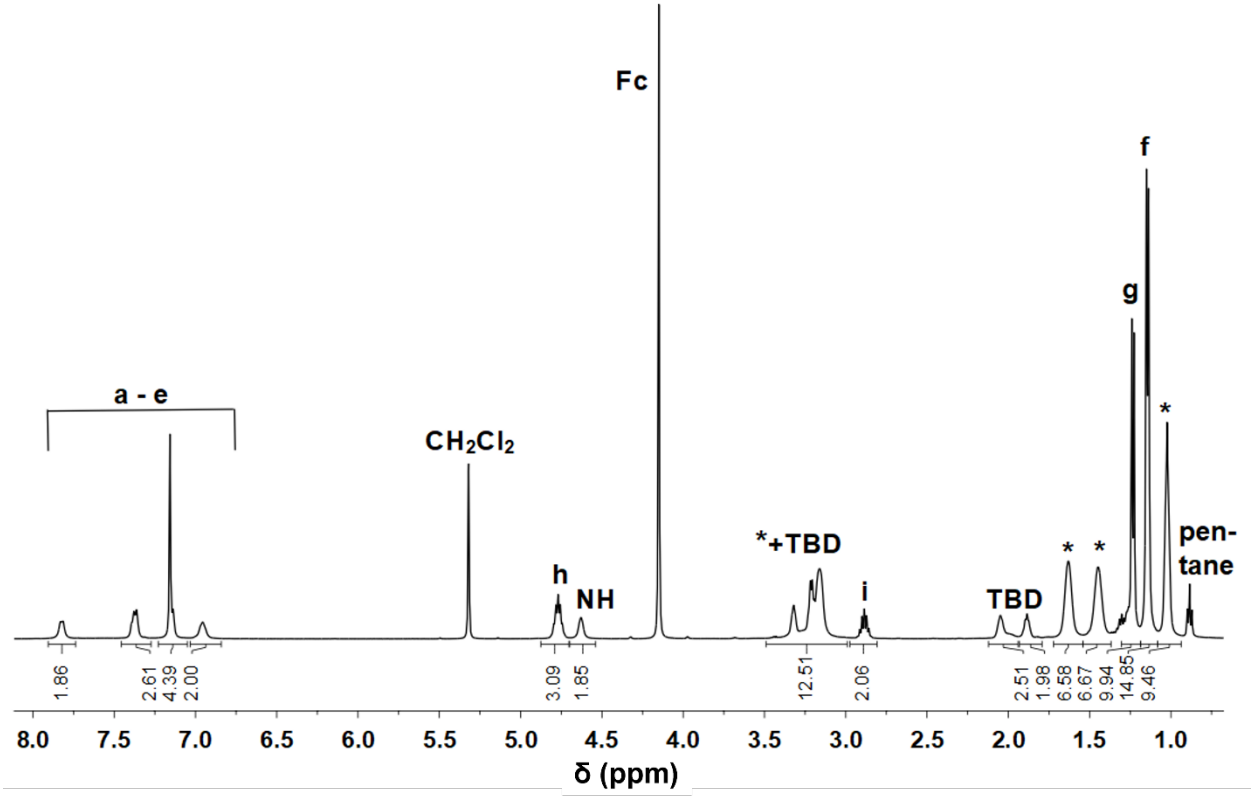

Figure S24. ^{1}H NMR spectrum of **2**-TBD. Conditions: collected in CD_2Cl_2 at room temperature using the CRYO500. Peaks arising from Bu_4N are represented by asterisk.

Aromatic protons were unable to be assigned other than the singlet with is attributed to "a". The NH proton was able to be assigned through a COSY correlation with the other features attributed to TBD. No NOESY correlations were observed.

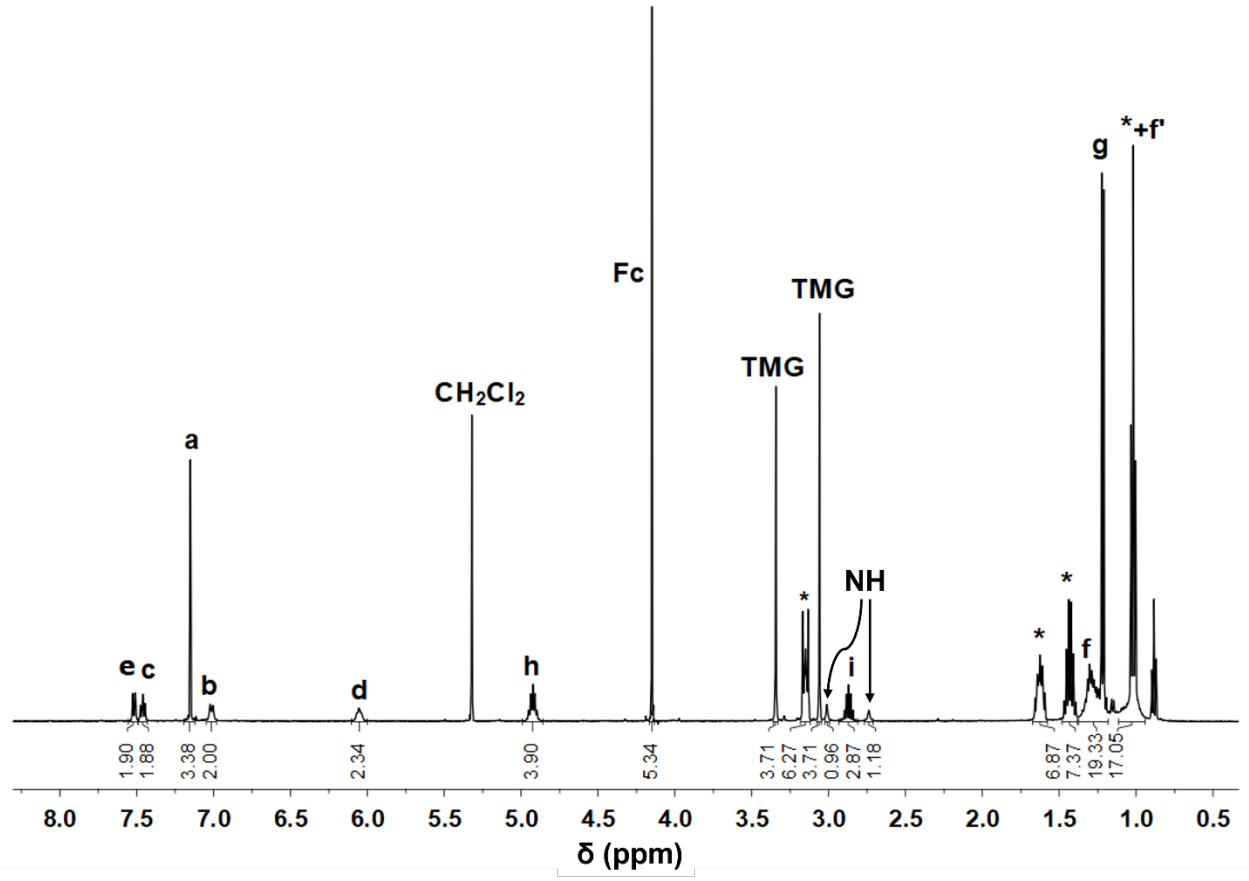

Figure S25. ^{1}H NMR spectrum of **2**-TMG. Conditions: collected in CD_2Cl_2 at room temperature using the CRYO500. Peaks arising from Bu_4N are represented by asterisk.

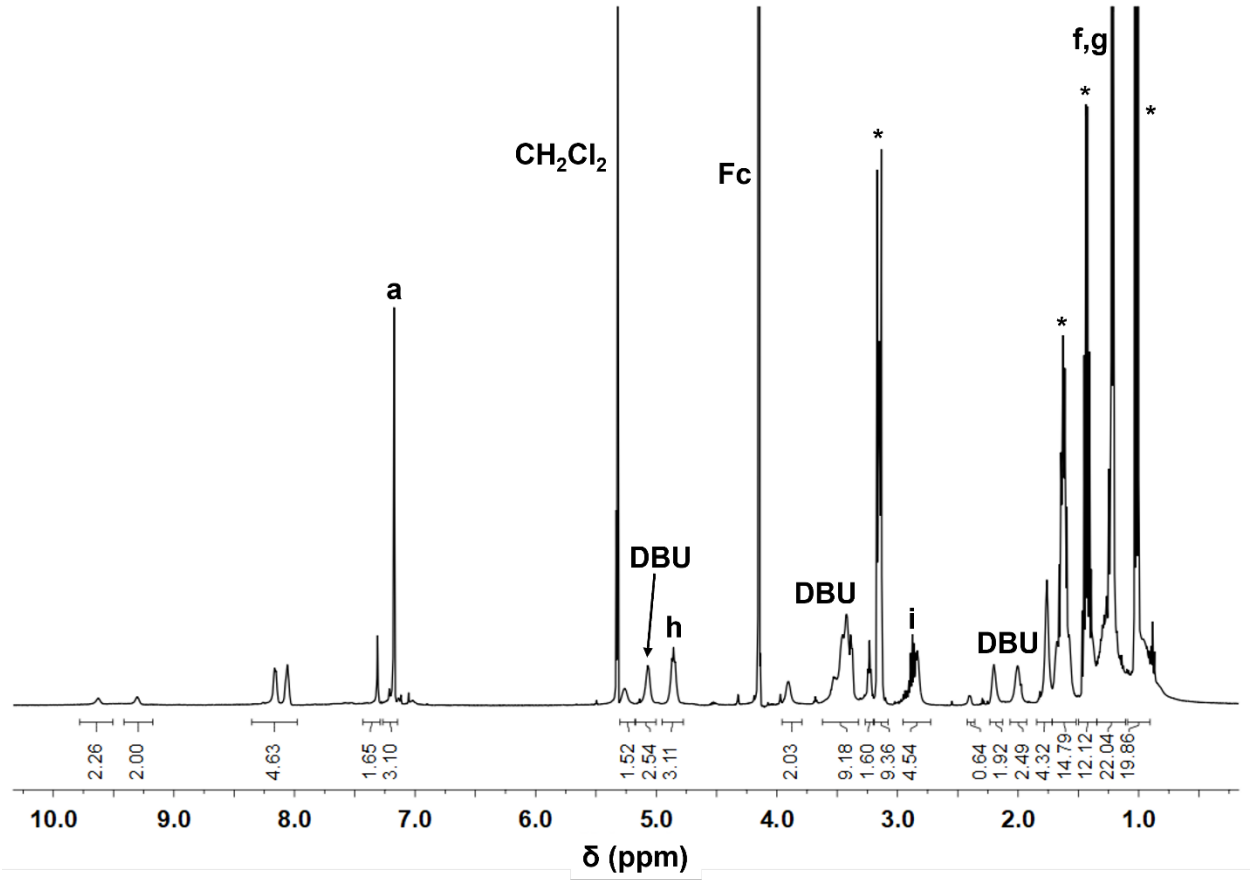

Figure S26. ^{1}H NMR spectrum of **2**-DBU. Conditions: collected in CD_2Cl_2 at room temperature using the CRYO500. Peaks arising from Bu_4N are represented by asterisk.

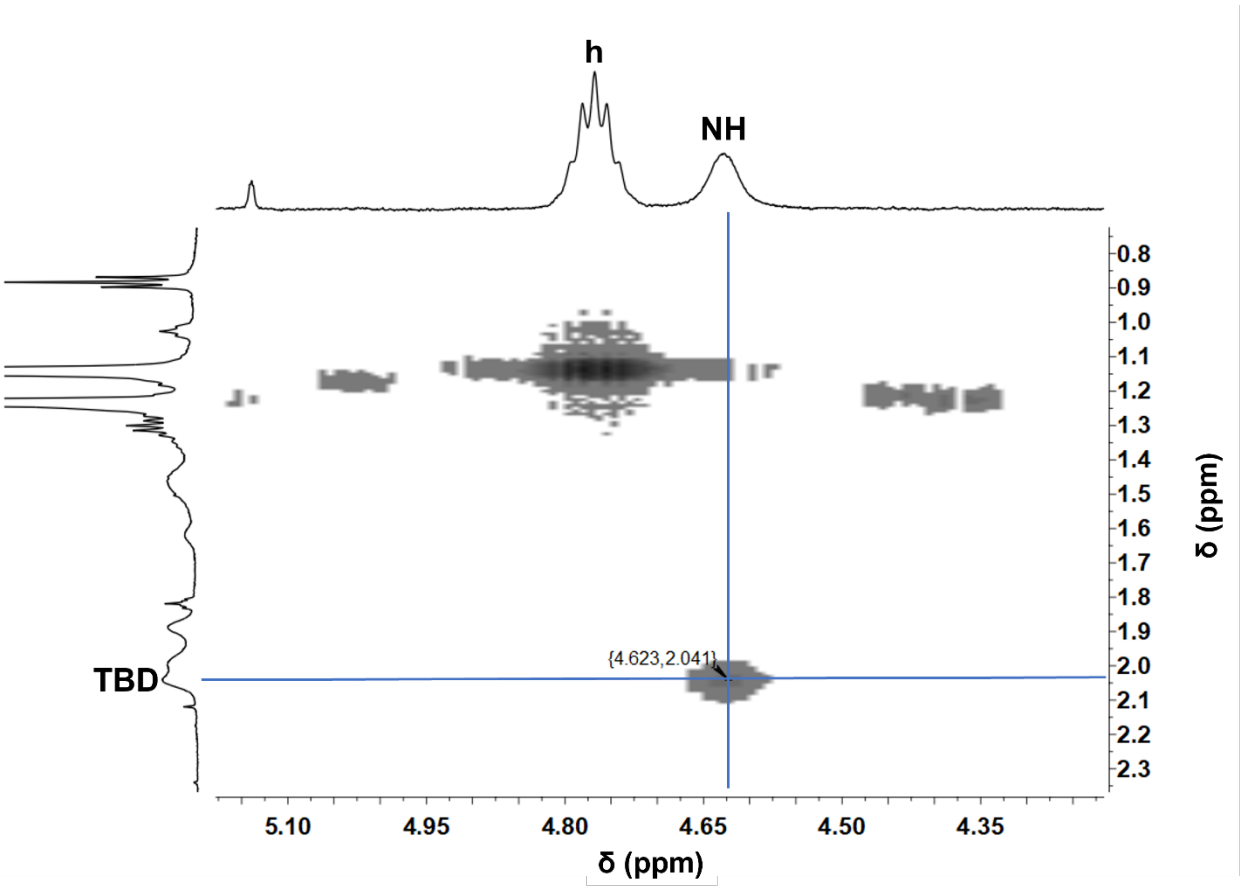

Figure S27. COSY NMR spectrum of **2**-TBD in the region showing the correlation between TBD and it's NH group.

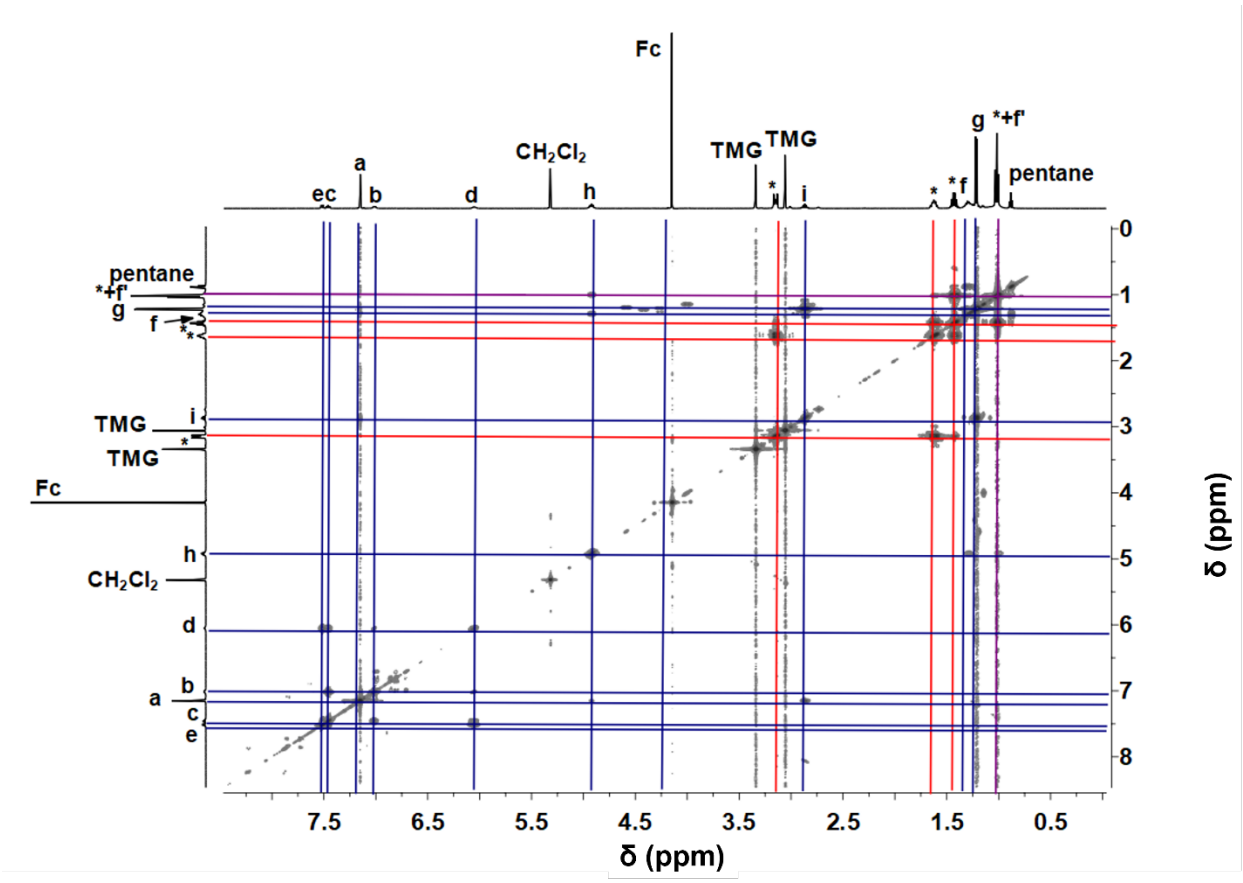

Figure S28. gCOSY NMR spectrum of **2**-TMG. Conditions: room temperature in CH_2Cl_2 using CRYO500. Blue lines represent correlation attributed to the anion and red represent the Bu_4N byproduct.

COSY correlations between **h** and features at 1.35 ppm and 1.08 suggest the *o*-methyl proton, **f**, gives rise to two signals (f and f'). One possibility for this unexpected occurrence is an H-bond between the sulfonamido oxygen atom and the hydroxido ligand causing the *o*-methyl protons to be inequivalent (this idea is further supported by Figure S29). The TMG protons likely give rise to the singlets between 2.5 and 3.5 ppm however this assignment remains uncertain. Signals from protons near the metal center shifted downfield from their location in the H_3ibaps as expected.

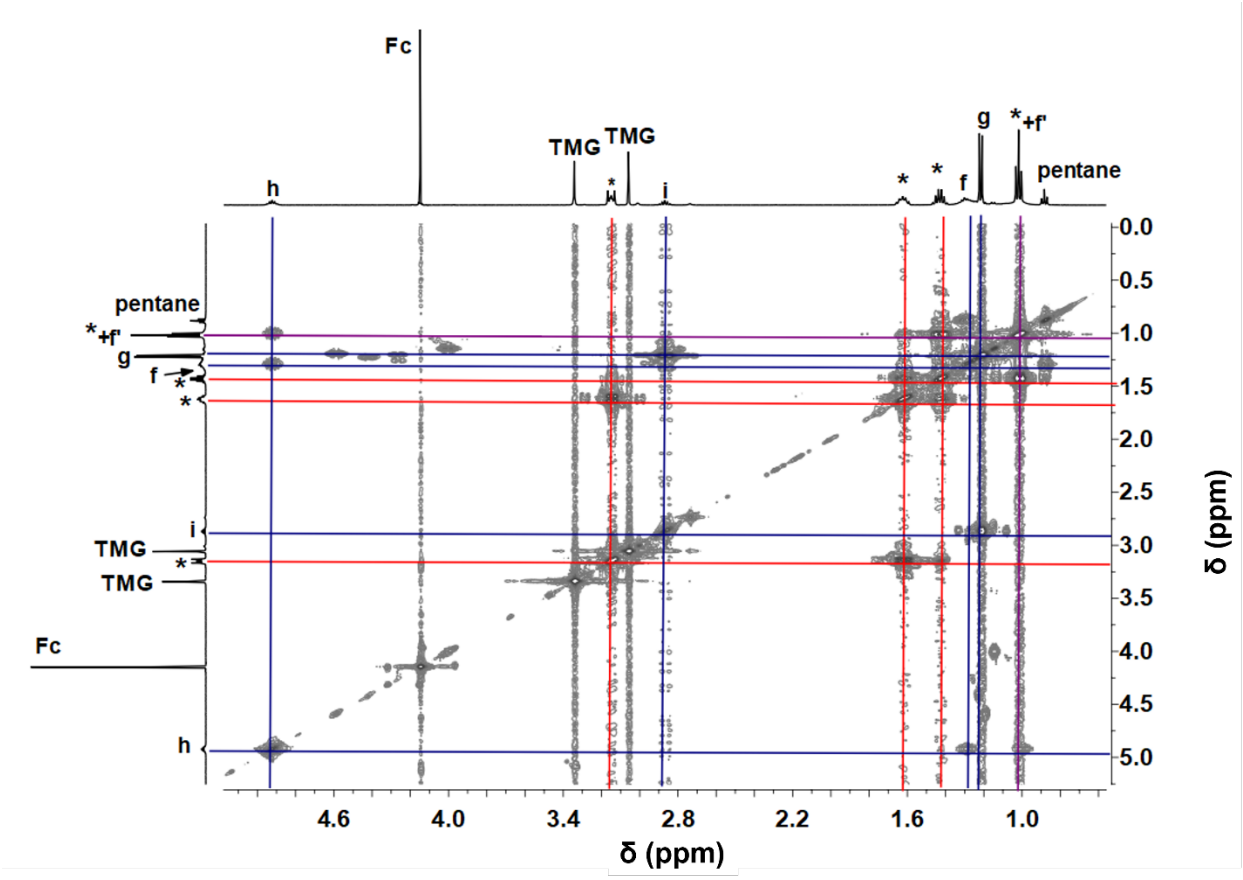

Figure S29. Upfield region of the gCOSY NMR spectrum of **2**-TMG. Conditions: room temperature in CH_2Cl_2 using CRYO500. Blue lines represent correlation attributed to the anion and red represent the Bu_4N byproduct.

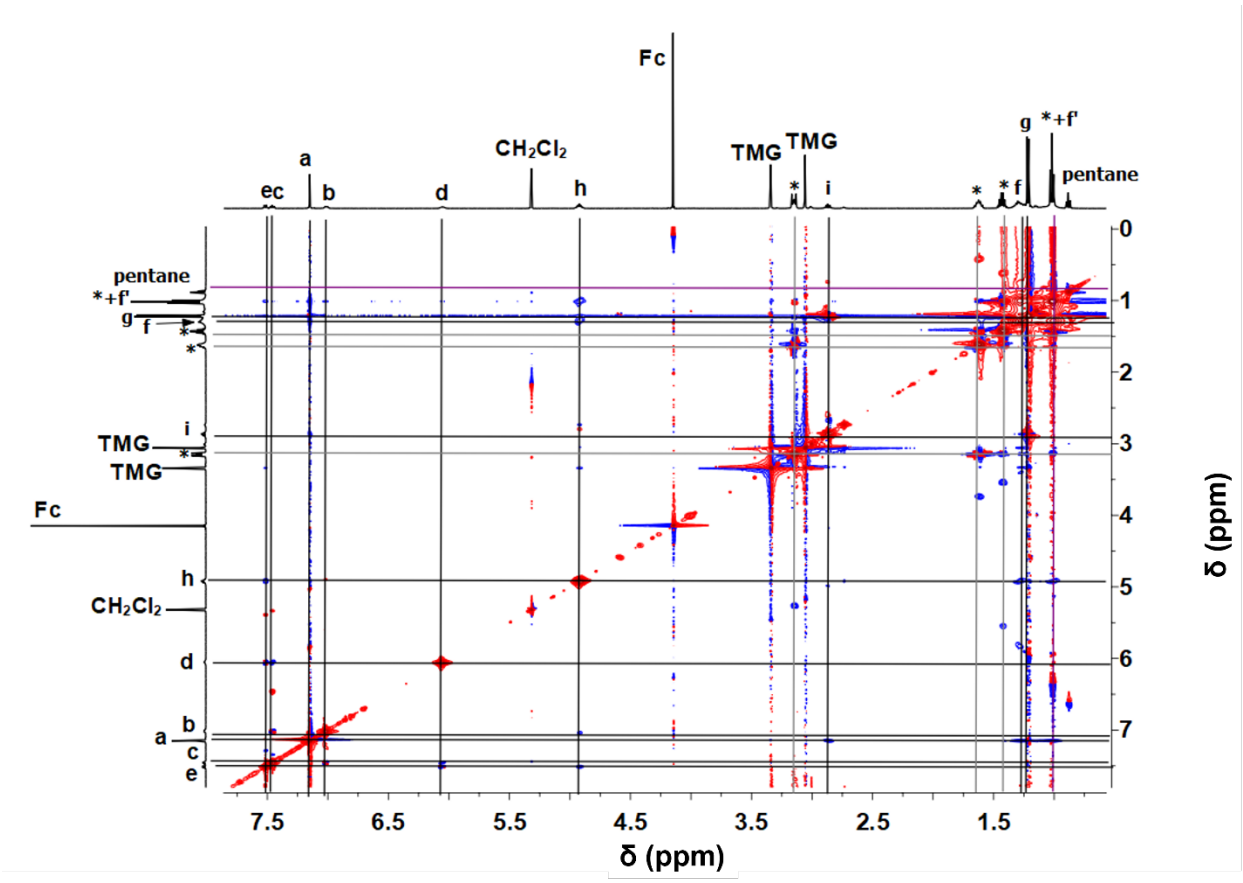

Figure S30. gNOESY NMR spectrum of **2**-TMG. Conditions: room temperature in CH_2Cl_2 using CRYO500. Black lines represent correlation attributed to the anion and gray represent the Bu_4N byproduct.

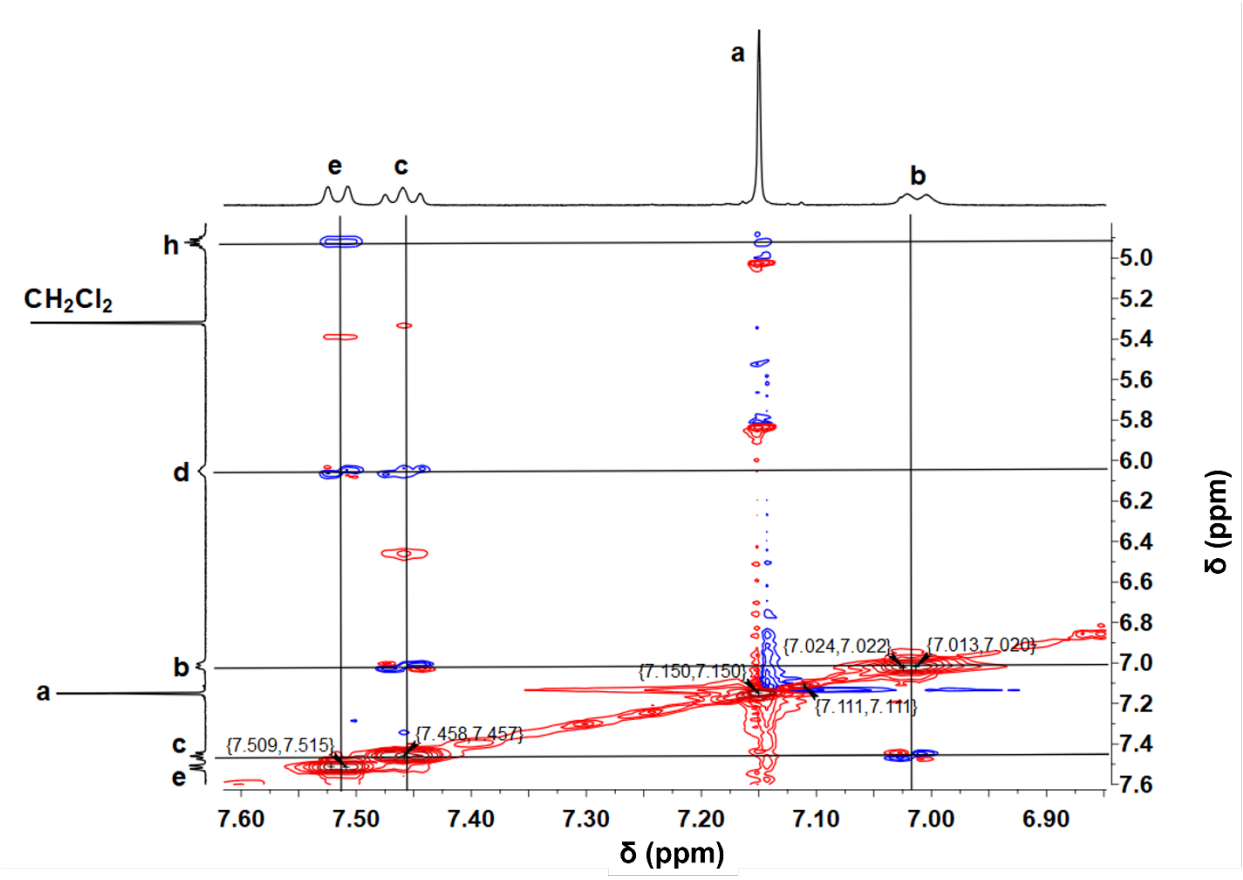

Figure S31. Aromatic region of the gNOESY NMR spectrum of **2**-TMG. Conditions: room temperature in CH_2Cl_2 using CRYO500.

NOE correlation between **h** (*o*-isopropyl methine) and **e** (*o*-CH with respect to substituted amine) allows for the identification of all aromatic protons within the ligand backbone. The doublet observed for **e** couples strongly with the septet of **h** indicates the p-isopropyl arm is within a close proximity to the backbone. **E**, now assigned to the *o*-CH with respect to the substituted amine, is observed to couple with NOE and COSY effects to the adjacent proton, **d**. **D** further couples with the remaining triplet peak in the aromatic region, **c**. **C**, finally, couples with b, the proton farthest from the o-isopropyl groups.

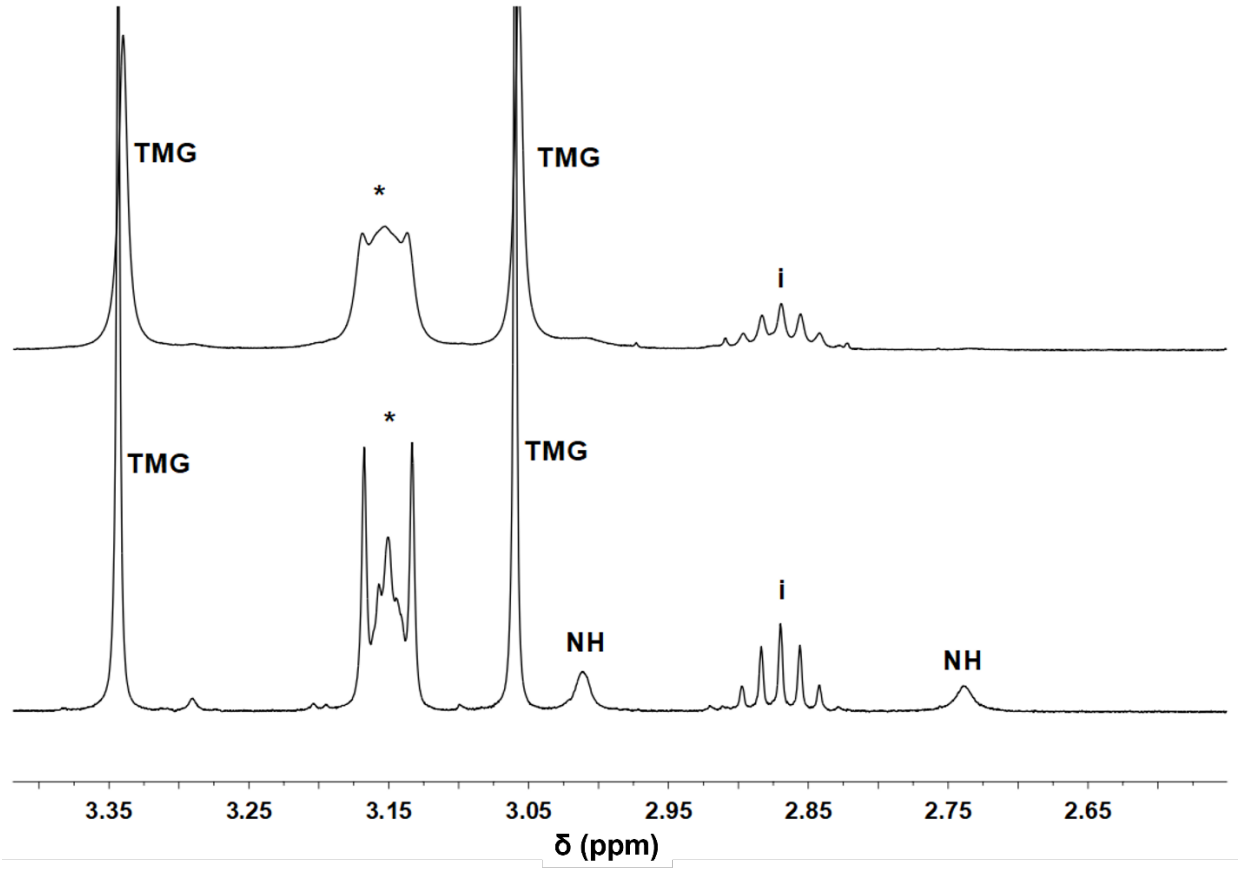

Figure S32. ^{1}H NMR spectrum of **2**-TMG (bottom) and **2**-TMG plus D_2O (top) between 2.5 and 3.4 ppm. Conditions: collected in CD_2Cl_2 at room temperature using the CRYO500. Peaks arising from Bu_4N are represented by asterisk.

Exchange of protons for deuterons resulted in loss of the features at 3.01 ppm and 2.74 ppm. The presence of two peaks attributed to the **NH** of TMG is likely due to a mixture of complex in which the TMG is H-bonded and not H-bonded in the solution state.

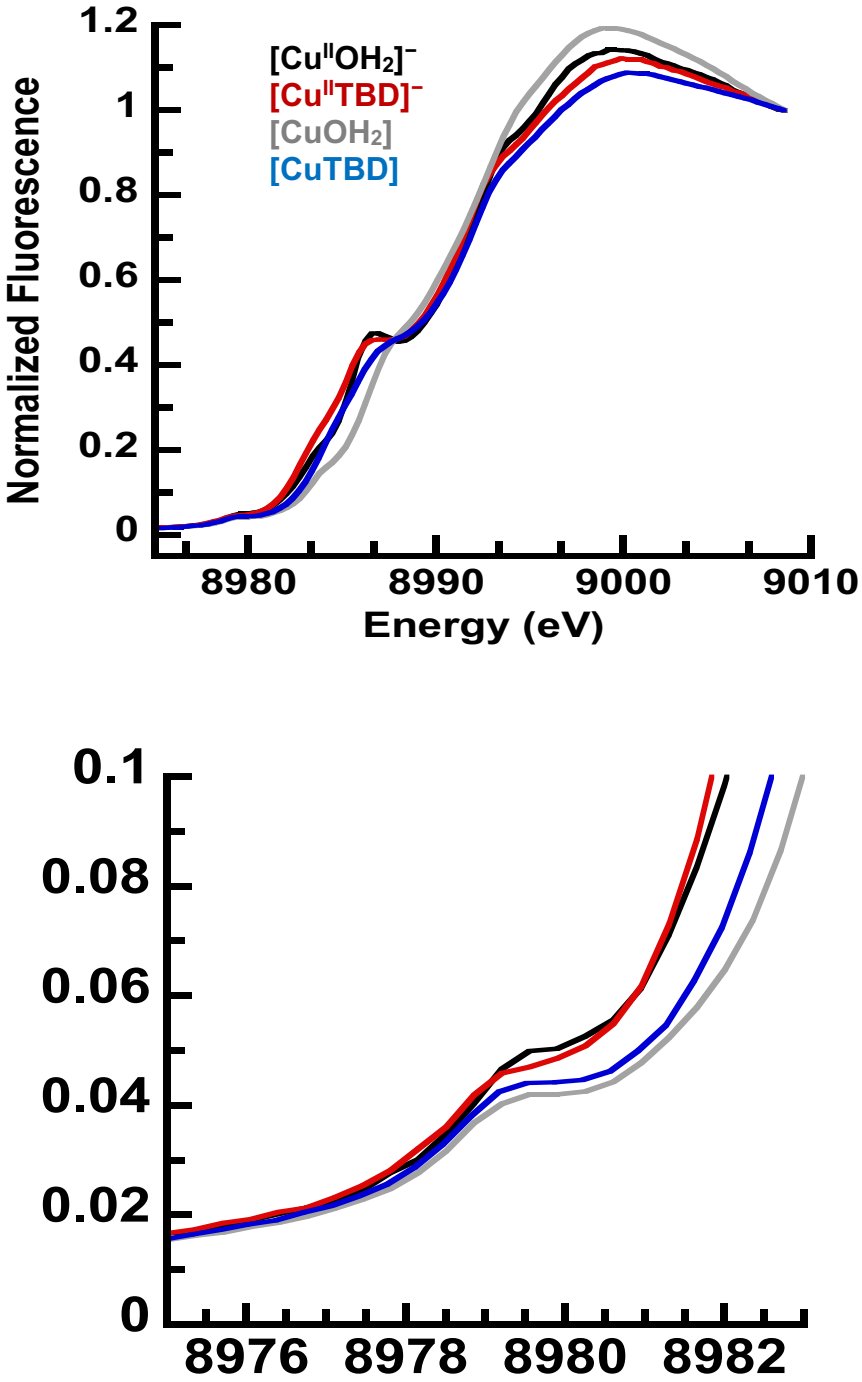

Figure S33. XANES data for **1**-OH_2, **1**-TBD, **2**-OH_2, and **2**-TBD. Bottom: zoom in of the 8976 – 8982 eV region where the pre-edge feature occurs.

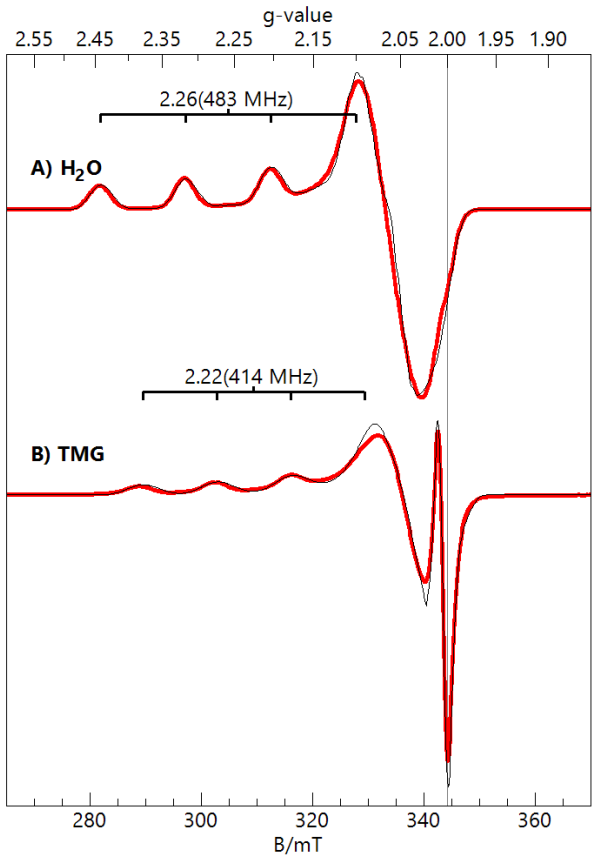

Figure S34. X-band (9.67 GHz, 0.2 mW) EPR spectra (red traces) and simulations (black traces) of **3**-OH_2 (A) and **3**-TMG (B) in DCM:THF. The simulation parameters are listed in Table 3. Sample temperature, 15 K.

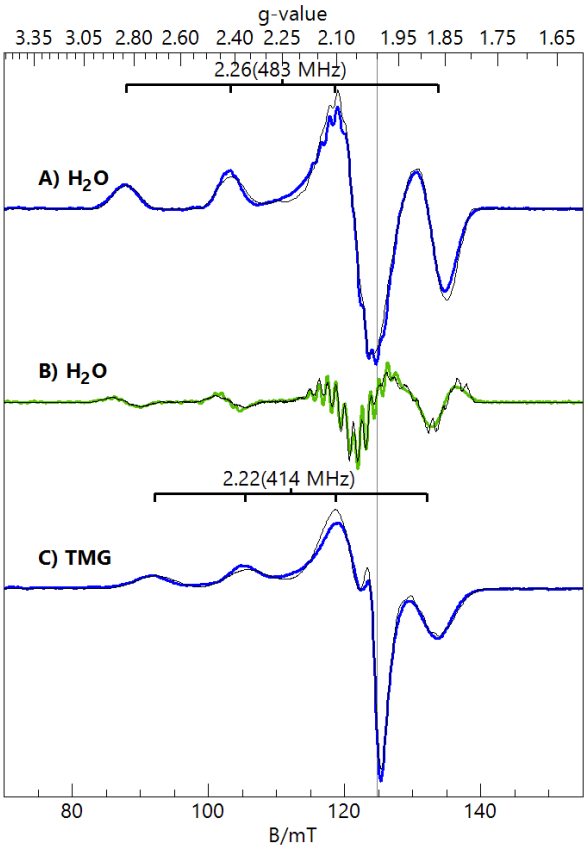

Figure S35. S-band (3.51 GHz, 0.03 mW) EPR spectra (blue/green traces) and simulations (black traces) of **3**-OH_2 (A) and **3**-TMG (C) in DCM:THF. The second derivative spectrum of **3**-OH_2 is shown in B. The simulation parameters are listed in Table 3. Sample temperature, 30 K.

Theoretical section

1. DFT analysis of g values of 1-OH₂.

Figure S34 presents the 3*d* energies and orbitals of a modified version of $[Cu^{II}(ibaps)OH_2]^-$ (methyl groups of the isopropyl groups are omitted) obtained from TD-DFT calculations. The dashed arrows indicate transitions of the spin-down electrons of the doubly occupied 3*d* orbitals into the singly occupied x^2-y^2 orbital, which are coupled by spin-orbit coupling to the ground configuration and contribute to the *g* values.

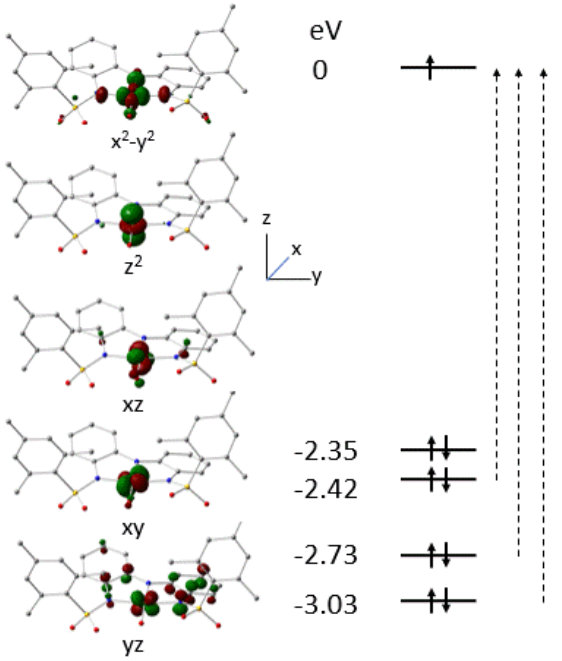

Figure S36. *d-d* transitions in a modified version of **1**-OH_2 (methyl groups of the isopropyl groups are omitted) from DFT calculations (B3LYP/Gen, Gen = 6-311G and TZVP on S). Energies and corresponding orbital contours are from TD-DFT. Dashed arrows indicate β electron transitions contributing to the g values.

The expressions for the *g* values are given by the following expressions,

$$g_x = 2\left(1 + \frac{\zeta}{\Delta_{yz \rightarrow x^2-y^2}}\right) \quad \text{(S1.1a)}$$

$$g_y = 2\left(1 + \frac{\zeta}{\Delta_{xz \rightarrow x^2-y^2}}\right) \quad \text{(S1.1b)}$$

$$g_z = 2\left(1 + \frac{4\zeta}{\Delta_{xy \rightarrow x^2-y^2}}\right) \quad \text{(S1.1c)}$$

where the denominators are the energies indicated in Figure S34. Using spin-orbit coupling constant ζ for Cu^{2+} of 839 cm^{-1}, one obtains g_x = 2.07, g_y = 2.09, and g_z = 2.30 compared to 2.03, 2.06, and 2.19 from EPR. DFT predicts the observed pattern of one large and two smaller g values. However, the calculated $\Delta g_\xi = g_\xi - 2$ values are ~ 30% larger than observed, due to either covalent reduction of the matrix element associated with the delocalization of the 3d orbitals onto the ligands (see Figure S34), effectively reducing the value of ζ in the above expressions, or to the underestimation of the energy denominators by TD-DFT. The analogous analysis of the $[Cu(ibaps)OH]^{2-}$ gives a similar level of agreement between theory and experiment.

2. *DFT analysis of g values of 2-OH_2.*

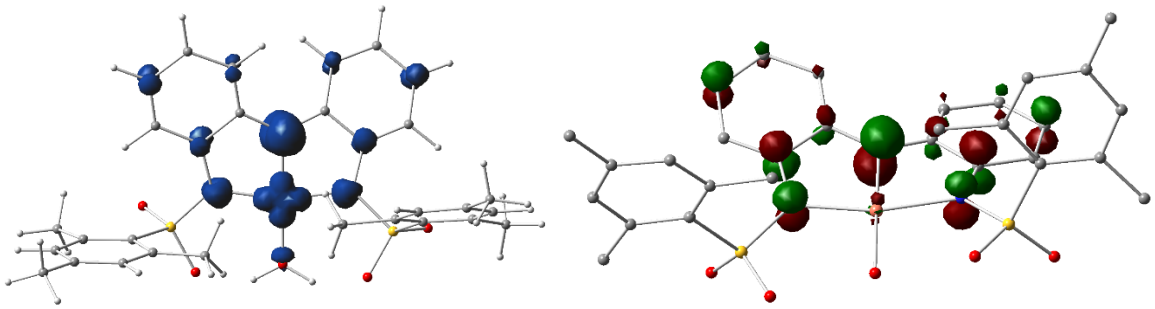

Figure S37. Spin density plots of a modified version of **2**-OH_2 (see above). Left. Spin density plot of B3LYP/Gen (6-311G and TZVP on S) solution for S = 1 optimized structure of a modified version of **2**-OH_2 (where the modification is the removal of the methyl groups on the isopropyl moieties). The spin populations reveal the contour of the unpaired electron carrying x^2-y^2 orbital of the Cu^{2+} site and the π_z-type radical orbital of truncated ibaps. Mulliken spin population (SP) of central nitrogen atom is 0.48, and SPs of left and right nitrogen atoms are 0.12. Right: Contour plot of the π_z-type ligand orbital carrying the unpaired ligand electron of **2**-OH_2. Hydrogen-atom have not been displayed for clarity. The vanishing of the overlap integral between the unpaired electron carrying orbitals, $\langle x^2 - y^2 | \pi_z \rangle \approx 0$, gives rise to a ferromagnetically coupled (S = 1) ground state.

The oxidized water complex has a set of *d-d* transitions like those in the reduced state with $\Delta_{yz \rightarrow x^2-y^2}$ = 2.87 eV, $\Delta_{xy \rightarrow x^2-y^2}$ = 2.73 eV, and $\Delta_{xz \rightarrow x^2-y^2}$ = 2.29 eV. These values are slightly smaller than the corresponding values for reduced form, with DFT predicted increases in Δg for Cu^{2+} site of about 5%. However, as the EPR analysis for the integer spin complex provides an incomplete set of g values, a verification of this trend is precluded.

3. *Analysis of A tensor of Cu^{2+} in series 1-X, X = H_2O, OH^-, TMG, and TBD.*

According to Hitchman[12] the isotropic component of the A tensor of a square planar Cu^{2+} complex with an unpaired electron in an x^2-y^2 orbital can be expressed as

$$A^{iso} = P\left\{-K\alpha^2 + \frac{1}{3}\left(\Delta g_x + \Delta g_y + \Delta g_z\right)\right\} \quad \text{(S3.1)}$$

where $K = 0.43$, α^2 and α'^2 are covalent reduction factors. P is a physical constant, taken as 1000 MHz for the **1-L** complexes. Δg_ξ (ξ = x, y, or z) is the difference $g_\xi - 2$, where g_ξ is an experimental g value obtained from EPR. The principal component of the traceless part (A^{tl}) of the A tensor along z, which has a negative value and is largest in magnitude ($|A^{tl}_z| > |A^{tl}_{x,y}|$), is given by

$$A^{tl}{}_z = P\left\{-\frac{4}{7}\alpha'^2 - \frac{5}{42}\left(\Delta g_x + \Delta g_y\right) + \frac{2}{3}\Delta g_z\right\} \quad \text{(S3.2)}$$

Table S6 gives the values of the Δg_ξ dependent terms in eqs S3.1 and S3.2 obtained from experimental g values. EPR gives only the magnitudes, not the signs, of the A tensor components. As A_z is negative from theoretical considerations, there are only four possible sign combinations for each complex. For each combination, the experimental A tensor has been decomposed in an isotropic component and a traceless component (Table S7). For each sign combination, the values for α^2 and α'^2 have been solved from eqs S3.1 and S3.2 and listed in Table S7. Using value of α'^2 thus obtained, $A^{SD,gs}{}_z$ is given by the value of the first term of eq S3.2 (gs refers to the ground state in the absence of spin-orbit coupling.)

The solutions in Table S7 that give a consistent trend in A^{iso} and an acceptable agreement with $A^{SD,gs}{}_z$ from DFT have been collected in Table S8.

4. Magnetochemistry of 1e-oxidized states (2-L).

The L-Cu-N angle (L = O or N) has important consequences for the magneto-chemical properties of the complexes. As illustrated in Figure 12 (left, top) linearity leads to the orthogonality of the orbitals containing the unpaired electrons. This, in turn, gives rise to a ferromagnetic exchange coupling ($J < 0$ using $J\widehat{\boldsymbol{S}}_1 \cdot \widehat{\boldsymbol{S}}_2$) according the Kanamori-Goodenough rules, leading to an $S = 1$ ground state. This situation is observed in **2**-H_2O complex, with DFT yielding $J \approx -900$ cm^{-1} and nearly identical optimized geometries for the F and BS states (Table 5). In contrast, bending of the L-Cu-N angle leads to the non-orthogonality of the unpaired electron containing orbitals (Figure 12 (left, bottom)) and consequently to antiferromagnetic exchange coupling ($J > 0$) according to these rules, resulting in an $S = 0$ ground state. The latter situation is found in the 1e-oxidized state of the other members of the **1-L** series. For example, DFT gives for **2**-DBU oppositely signed J values of −235 cm^{-1} and +5900 cm^{-1} for the optimized geometries of the F and BS states, respectively. The dramatic change in the J value is due to the change in the L-Cu-N angle from nearly linear to bent. By suppressing the $\pi - x^2$-y^2 transfer driven bending mechanism, hydrogen bonding has turned **2**-H_2O into a unique member of the **2**-L series.

BS calculations are nowadays routinely used for the calculation of the coupling constants (J) of the "super" exchange interactions mediated by the bridging ligands in binuclear transition metal complexes with paramagnetic metal sites. The optimized geometries for the BS and F states for the super-exchange coupled complexes are often virtually identical and the orbitals containing the unpaired electrons change little between the two states. Under these conditions, the energy of the BS state for two $S = ½$ sites is halfway the energies for the $S = 1$ and $S = 0$ states, $E_{BS} = (E_F + E_{S=0})/2$. Using the convention $J\widehat{\boldsymbol{S}}_1 \cdot \widehat{\boldsymbol{S}}_2$, the exchange-coupling constant J can then be expressed as $J = 2(E_F - E_{BS})$ and the energy of the true $S = 0$ state is then given by $E_{S=0} = E_{BS} - J/2$. However, the weak-coupling conditions are not fulfilled in the imine complexes of the 1e-oxidized **2-L** series, because the direct overlap of the unpaired electron orbitals gives stronger interactions than typically found the super exchange complexes, leading to large changes in the structure, such as in the L-Cu-N angle, in passing from the F state to the BS state (Table 5). In the strong coupling case, the quantity ΔE listed

in Table 5 is not a pure exchange energy but also contains contributions from geometry and orbital changes. As the energy of the $S = 0$ state is lower than the energy for the BS state, the quantity ΔE listed in Table 5 is smaller than the energy separating the F state from the true $S = 0$ state. Using as a first approximation the expression for weak coupling, the correction amounts to $-J/2$, with J being the exchange-coupling constant between the unpaired electrons at the Cu and [ibaps]$^{3-}$ ligand, obtained from the DFT energies for the F and BS states at the optimized geometry for the BS state: $J = 2[E_F(\text{BS geo}) - E_{BS}(\text{BS geo})]$. Taking the **2**-DBU complex as an example, the J value was calculated to be 5900 cm^{-1}, resulting in the energy difference $E_F(\text{F geo}) - E_{S=0}(\text{BS geo}) = 3500$ cm^{-1}, representing a significant increase compared to the quantity $\Delta E = E_F(\text{F geo}) - E_{BS}(\text{BS geo}) = 560$ cm^{-1} listed in Table 5 The above treatment, however, may have overestimated the correction because of orbital state changes. The antiferromagnetic coupling arises from the admixture of the two-electron ground configuration, $|(x^2\text{-}y^2)\pi(\alpha\beta-\beta\alpha)|$, with the excited charge-transfer configuration $\pi\pi(\alpha\beta-\beta\alpha)$ and, possibly, also $(x^2\text{-}y^2)\,(x^2\text{-}y^2)(\alpha\beta-\beta\alpha)$. The above relations between E_{BS}, E_F and $E_{S=0}$ are only valid when these admixtures are small. However, for larger admixtures as in the case of the imine complexes, E_{BS} approaches $E_{S=0}$, reducing the difference between $E_{S=0}$ and E_{BS}, with equality being reached when the two electrons occupy one orbital, $\varphi\varphi(\alpha\beta-\beta\alpha)$. The value for $E_F(\text{F geo}) - E_{S=0}(\text{BS geo})$ is thus somewhere between 560 cm^{-1} and 3500 cm^{-1}. The ratio of the $A^{SD}{}_z$ values from the BS and F calculations for **2**-DBU is about 0.7 and measures to what extent the copper spin has been paired off by the $\pi - x^2\text{-}y^2$ transfer in the BS state. By scaling the correction $-J/2$ with this factor yields a correction of 2000 cm^{-1} (0.25 eV) and results in the gap $E_F(\text{F geo}) - E_{S=0}(\text{BS geo}) = 2600$ cm^{-1} between the energies for the spin-state optimized geometries.

5. DFT analysis of electrochemical data.

DFT calculations have been used to predict trends in midpoint potentials based on the electronic energies of the complexes. The potentials for the first and second oxidation step of the **1-L** complexes have been expressed as $E_{1/2}(\text{L}) = C + E_{ox}(\text{L}) - E_{red}(\text{L})$ and $E'_{1/2}(\text{L}) = \text{C} + E_{2ox}(\text{L}) - E_{ox}(\text{L})$, respectively, where C is an electrode-dependent constant, and $E_{red}(\text{L})$, $E_{ox}(\text{L})$, and $E_{2ox}(\text{L})$ are the DFT system energies of the complex **1-L** in the reduced state, the 1e-oxidized state, and the 2e-oxidized state, respectively. The DFT energies are negative and appear in the order $E_{red}(\text{L}) < E_{ox}(\text{L}) < E_{ox\text{-}ox}(\text{L})$. E_{ox} is here defined as the energy of the state with the lowest energy among the F and BS states. To eliminate constant C from the analysis, we defined the quantities $\Delta E_{1/2}(\text{L}) = E_{1/2}(\text{L}) - E_{1/2}(\text{H}_2\text{O})$, $\Delta E'_{1/2}(\text{L}) = E'_{1/2}(\text{L}) - E'_{1/2}(\text{H}_2\text{O})$, and $E'_{1/2}(\text{L}) - E_{1/2}(\text{L}) = E_{red}(\text{L}) - 2\,E_{ox}(\text{L}) + E_{2ox}(\text{L})$. The computational results for these quantities are listed in Table S4 for the **1-L** complexes in gas phase and in DCM solution. The experimental values are given in parentheses for comparison.

The DFT calculations for L = TMG, TBD, and DBU predict negative $\Delta E_{1/2}$ and $\Delta E'_{1/2}$ values both in gas phase and solution, indicating that the redox active electrons in these complexes are less tightly bound than in the H_2O complex. The $\Delta E_{1/2}$ values from DFT are in reasonable agreement with the experimental values. Less satisfactory agreement is found for $\Delta E'_{1/2}$. While the solvent has only a moderate influence on the $\Delta E_{1/2}$ and $\Delta E'_{1/2}$ values, its effect on $E'_{1/2}(\text{L}) - E_{1/2}(\text{L})$ is significant. The charge of the complexes changes from −1 to 0 to +1 in the two oxidation steps. As the solvation energy contributions associated with these electric monopole changes are approximately equal for all four complexes, they mutually cancel in the expressions for $\Delta E_{1/2}$ and $\Delta E'_{1/2}$, causing only modest changes in these quantities in passing from gas phase to solvent. In contrast, considering that the E_{red} and E_{2ox} terms in the expression for $E'_{1/2}(\text{L}) - E_{1/2}(\text{L})$ are lowered by monopole solvation energies

while the term E_{ox} for the electrically neutral state is not, the value for $E'_{1/2}(L) - E_{1/2}(L)$ in solution is significantly lower than in gas phase.

To account for the difference between the BS state and the true $S = 0$ state (see above), the DFT values for $\Delta E_{1/2}(L)$ and $\Delta E'_{1/2}(L)$ (L = TMG, TBD, or DBU) listed in Table S4 must be corrected by adding the term $E_{S=0}(L) - E_{BS}(L) < 0$. Since the 1e-electron oxidized BS state acts as the oxidized state of the first redox couple and as the reduced state of the second redox couple, the values for $\Delta E_{1/2}(L)$ and $\Delta E_{1/2}(L)$ are, respectively, lowered and raised by the correction. Using the above example of **1-DBU** for which the correction was estimated to be −0.25 eV (see above) the corrected values in DCM solution are $\Delta E_{1/2}(DBU) = -0.52$ eV and $\Delta E'_{1/2}(DBU) = +0.08$ eV. While both the nearly vanishing potential shift for the second oxidation step and the negative sign of the shift for the first oxidation step agree with experiment, the magnitude of the latter has been overestimated by the calculations.

The DFT data in Tables 5 and S7 show that the non-planarity (L-Cu-N < 180°) of the coordination geometries in the TMG, TBD and DBU complexes correlates with a negative shift in the potential $E_{1/2}$ relative to the nearly planar H_2O complex (L-Cu-N ≈ 180°). The negative shift arises from a lowering in the value for $E_{ox} - E_{red}$ (> 0) occurring in tandem with the decrease of the L-Cu-N bond angle. The $\pi - x^2\text{-}y^2$ resonance interaction, which is absent in **1-H_2O** complex but present in the other three complexes, is a plausible contributor to the shift. However, since this resonance interaction is present in both the reduced and 1e-oxidized BS states the energy difference $E_{ox} - E_{red}$ is not affected unless the resonance stabilization energies are different in the two oxidation states. To give a rough estimate of this difference we have performed DFT calculations for **1-DBU**, thereby avoiding the complexities arising from hydrogen bonding in the other two imine complexes. First, we evaluated the exchange-coupling constant for the optimized geometry in the BS state of the 1e-oxidized complex, which has L-Cu-N = 143°, and obtained $J = 5900$ cm^{-1} (see above). Second, we evaluated an exchange-coupling constant for the 1e-oxidized state using the optimized geometry of the reduced state, which has L-Cu-N = 147°, by removing an electron from the ligand π orbital at fixed reduced-state geometry and taking twice the difference of the F and BS state energies obtained from single point calculations, $J_{red} = 2[E_F(\text{red geo}) - E_{BS}(\text{red geo})]$. The latter calculation yielded $J_{red} = 3300$ cm^{-1}. The difference of the two J values (0.3 eV) is measure for the increase in resonance stabilization in the 1e-oxidized BS state relative to the reduced state. As this resonance stabilization is absent in **1-H_2O**, the $E_{1/2}$ value for **1-DBU** has undergone a negative shift relative to **1-H_2O** (Table S4). Alternately, considering that the oxidations are ligand based, we have also investigated whether the shift in $E_{1/2}$ could be due to differences between in the structures of the ibaps ligand in the optimized **1-H_2O** and **1-DBU** structures. However, the DFT calculations suggest that these structural changes are too small to produce the $\Delta E_{1/2}$ values listed in Table S4.

6. DFT structures of complexes with truncated [ibaps]$^{3-}$ ligand.

For the TBD complex, **1-TBD**, the sulfonamido side chains keep the plane of TBD perpendicular to the ibaps plane, whereas for the truncated structure, $[Cu(ibaps^T)TBD]^{1-}$, the optimization tilted the TBD plane to approximately align with that of the CuN_3L core. To mimic the perpendicular TBD orientation for the truncated structure, the optimizations for the two imine-type complexes (TBD and CH_2NH) in Table 5 were performed with the imine constrained to be perpendicular to the CuN_3L plane. Table 5 shows that, like for the ibaps structures, the complexes with the additional N donor result in structures having L-Cu-N angles significantly less than 180°. For

those complexes with smallest L-Cu-N angle, the N2-Cu-N3 angle also reduces, giving a non-planar CuN_3L unit with an imperfect tetrahedral distortion.

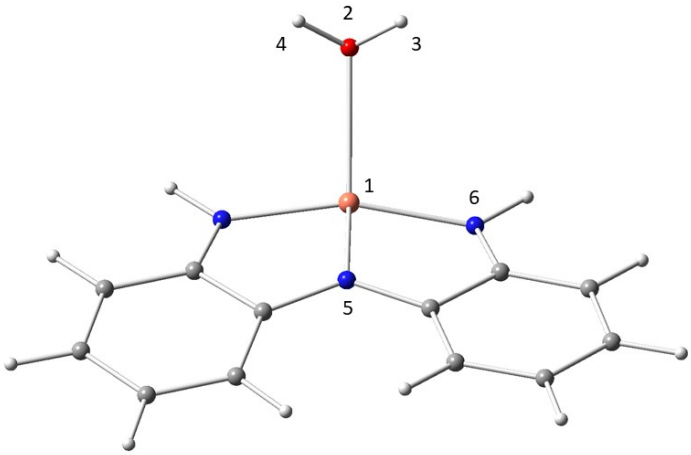

Figure S38. DFT structure obtained from constrained geometry optimization of $[Cu(ibaps^T)OH_2]^{1-}$. During the optimization, one of the sp^3 lone pairs of the water ligand has been kept directed toward the Cu by fixing the angles 3-2-1 and 4-2-1 and the oxygen is kept in the plane through 1-5 perpendicular to $ibaps^T$ by fixing the dihedral angle 2-1-5-6. Angle 2-1-5 is 131°. Color scheme: H (white), C (grey), N (blue), O (red), and Cu (orange).

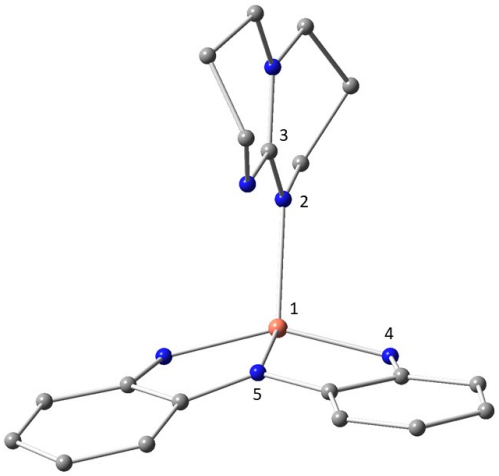

Figure S39. DFT structure obtained from constrained geometry optimization of $[Cu(ibaps^T)TBD]^{1-}$. The TBD ligand is kept in perpendicular alignment to the $ibaps^T$ plane by fixing the dihedral angle 3-2-1-4. Angle 2-1-5 is 123°. Color scheme: C (grey), N (blue), O (red), and Cu (orange). H atoms are not shown for clarity.

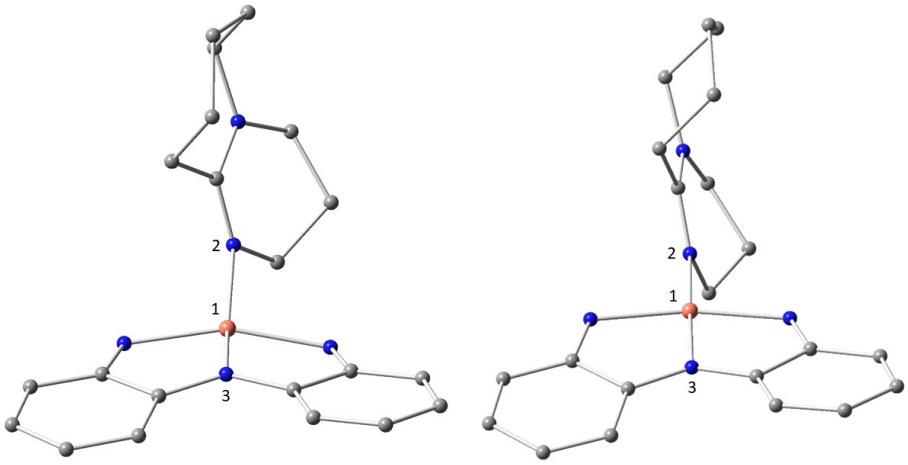

Figure S40. DFT structures of $[Cu(ibaps^{T})DBU]^{1-}$ (left) and the S = 1 state of $[Cu(ibaps^{T})DBU]^{0}$ (right). Angles 2-1-3 are 159° (left) and 179° (right). Color scheme: C (grey), N (blue), O (red), and Cu (orange). H atoms are not shown for clarity.

7. DFT structures of the 3-L Complexes.

For the two-electron-oxidized complexes (**3**-L), DFT results gave different L-Cu-N1 angles for the Cu complexes with $[ibaps]^{1-}$ versus $[ibaps^{T}]^{1-}$ ligands (Table S9). For the $\mathbf{3}^{T}$-L complexes, the now-empty π orbital cannot donate into the Cu d_{x2-y2} orbital, resulting in L-Cu-N1 angles of nearly 180°. The same angle computed for the **3**-L complexes deviates from linearity with angles between 149° and 172°; thus, the calculations of these complexes indicate that the imine ligands have either steric or H-bond interactions that also contribute to the smaller L-Cu-N1 angles.

The two-electron oxidation of **1**-L removes two electrons from the HOMO π orbital of $[ibaps]^{3-}$, leaving this orbital unoccupied in the **3**-L complexes. The d-p_z bonding described in Figure 12 is then absent, and the complex cannot lower its energy by decreasing the L-Cu-N1 angle. Thus, the DFT calculations for the truncated $\mathbf{3}^{T}$-L complexes gave L-Cu-N1 angles that are nearly linear. However, our DFT calculations for the **3**-imine complexes gave nonlinear L-Cu-N1 angles (Table 5). Furthermore, the experimental A_{iso} and A_z values for the Cu center in **3**-TMG were lower than the values for **3**-OH_2, and the A_z^{SD} values agree with the DFT-calculated values (Tables 3 and 6). The L-Cu-N1 angle in the **3**-L complexes may have become more susceptible to steric influences than in the **1**-L complexes, as the two-electron oxidation of the ligand has lessened the σ donations that stabilize the square planar coordination geometry. The lower σ electron donation and the accompanying increase in the spin population of the Cu^{II} site is in keeping with the increase in the P value for the two-electron-oxidized complexes that was noted above.

8. TD-DFT analysis of electronic absorption spectra.

The results for the electronic absorption spectra obtained from time-dependent (TD) DFT calculations for the reduced **1**-H_2O and **1**-TMG complexes, displayed in Figures S39 and S40 show that the seven lowest energy transitions in both species involve the transfer of an electron into the

vacant x^2-y^2 orbital of the copper. In the first and second lowest energy transitions an electron is excited from the ligand π and π_- orbitals, respectively, where π is the redox active ibaps orbital with a large p_z component at the central coordinating nitrogen atom and π_- is the combination $p_z(N') - p_z(N'')$ of the p_z orbitals at the coordinating N' and N'' atoms left and right of the Cu, with z being aligned normal to the ibaps plane. The next five transitions are $d \rightarrow x^2$-y^2 admixed with ligand → metal transitions, predominantly $\pi_+ \rightarrow x^2$-y^2, with $\pi_+ = p_z(N') + p_z(N'')$, leading to higher absorptivity than typically observed for $d \rightarrow d$ transitions. Next lowest in energy is a set of ligand → ligand transitions of the form $\pi \rightarrow \pi_R$ in which an electron is transferred from the ibaps moiety to the sidechain rings, labeled R. Overall, the absorption above 400 nm in **1**-TMG is larger than in **1**-H_2O, which we ascribe to a higher degree of non-planarity in the Cu coordination of the former complex. A comparison with the electronic absorption spectra recorded for the two species shows that a similar intensity difference is observed in experiment. Also, the band positions on the wavelength scale have been reasonably well predicted by the TD-DFT calculations of the two species, except for the lowest energy transition which is calculated to be somewhat further out in the IR than observed.

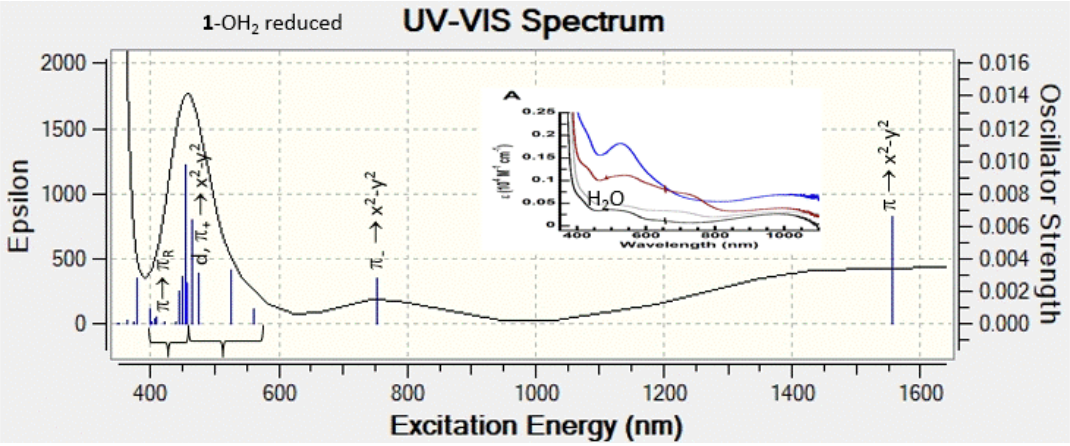

Figure S41. Electronic absorption spectrum for **1**-H_2O from B3LYP/TZVP TD-DFT calculations. The right-hand axis gives the scale for the oscillator strengths of the stick spectrum. The left-hand axis gives the scale of the absorptivity in M^{-1} cm^{-1} units. The spectrum (black solid curve) was constructed from the stick spectrum using a line width parameter of 0.2 eV. Transitions with wavelengths > 400 nm have been assigned based on analysis of the TD transitions. The inset gives the experimental spectra for reduced form of **1**-**L**, with L = H_2O in black, DBU in gray, TBD in maroon, and TMG in blue. R labels the rings of the side chains in the ibaps ligand, R-S(O_2)-N'-Phen-N-Phen-N''-(O_2)S-R. π labels the redox active HOMO of ibaps of which the largest amplitude is at the coordinating central nitrogen.

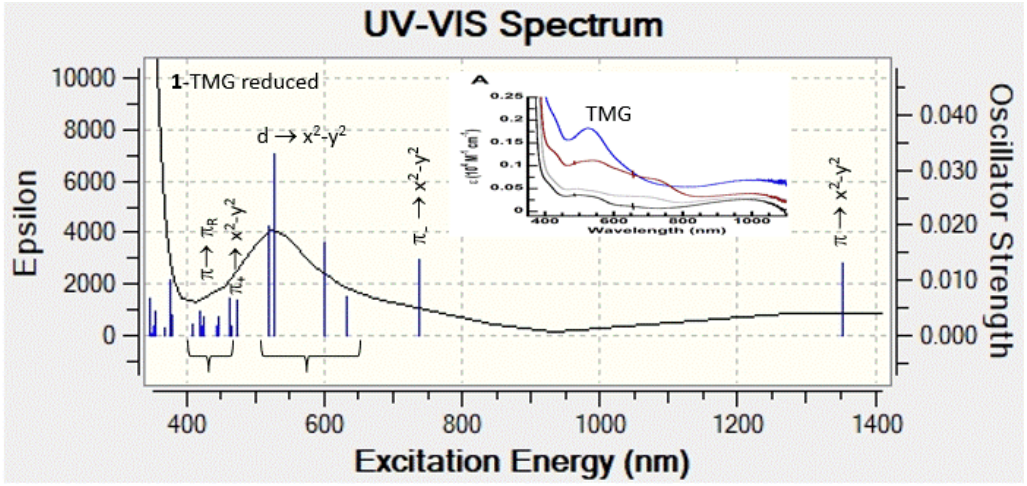

Figure S42. Electronic absorption spectrum for the reduced **1**-TMG complex from B3LYP/TZVP TD-DFT calculations. The right-hand axis gives the scale for the oscillator strengths of the stick spectrum. The left-hand axis gives the scale of the absorptivity in M^{-1} cm^{-1} units. The spectrum (black solid curve) was constructed from the stick spectrum using a line width parameter of 0.2 eV. Transitions with wavelengths > 400 nm have been assigned based on analysis of the TD transitions. The inset gives the experimental spectra for reduced form of **1**-L, with L = H_2O in black, DBU in gray, TBD in maroon, and TMG in blue. R labels the rings of the side chains in the ibaps ligand, R-S(O_2)-N'-Phen-N-Phen-N"-(O_2)S-R. π labels the redox active HOMO of ibaps of which the largest amplitude is at the coordinating central nitrogen.

The 1e- and 2e-oxidations of the **1-L** complexes, in which electrons are removed from the π orbital, introduces additional transitions in the visual range in which an electron is transferred into the vacated π orbital. For example, the number of TD transitions with wavelength greater than 400 nm increases from 16 in **1**-H_2O to 29 in 2e-oxidized **1**-H_2O, leading to a significant increase in absorptivity in the visual range as can be seen from the TD-DFT derived spectrum shown in Figure S41. A comparison of the spectra for the reduced and oxidized states of **1-L** shown in Figure 5 reveals a similar increase in the experimental data for the oxidized states.

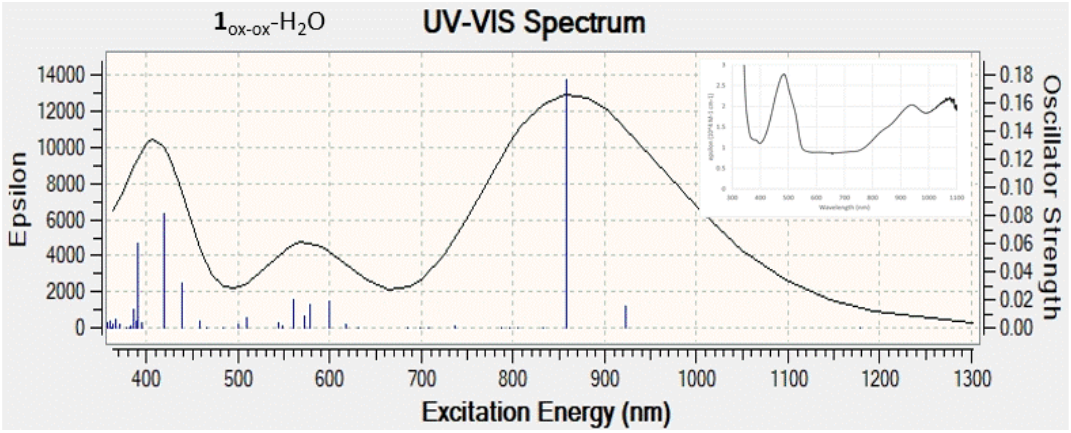

Figure S43. Electronic absorption spectrum for the 2e-oxidized **3**-H_2O from B3LYP/TZVP TD-DFT calculations. The right-hand axis gives the scale for the oscillator strengths of the stick spectrum. The left-hand axis gives the scale of the absorptivity in M^{-1} cm^{-1} units. The spectrum (black solid curve) was constructed from the stick spectrum using a line width parameter of 0.2 eV. The inset gives the experimental spectrum for 2e-oxidized **3**-H_2O.

The water-coordinated Cu complex, **4**-H_2O, supported by the tridentate ligand N,N'-bis(2,6-diisopropylphenyl)-2,6-pyridinedicarboxamide, reported by Tolman and coworkers has a planar coordination in spite of lacking any planarity enforcing hydrogen bonds as present in **1**-H_2O. A planar coordination geometry is also found in the DFT optimized structures of **4**-H_2O and **4**-TBD, raising the question as to why the bending-driving $\pi \rightarrow x^2\text{-}y^2$ mechanism acting in **1**-L is not operative in **4**-H_2O. We think the difference between the coordination geometries of the **1**-L and **4**-L complexes is rooted in the nature of the central coordinating nitrogen atom, viz. an imine nitrogen with a rather localized p_z-like π orbital with high energy in **1**-L and a pyridine nitrogen of which the p_z orbital is a component of the delocalized π orbitals that are much lower in energy in **4**-H_2O. The resulting increase in the energy gap between the π orbital and the $x^2\text{-}y^2$ orbital inactivates the $\pi \rightarrow x^2\text{-}y^2$ bending mechanism in **4**-H_2O. This explanation for the linearity of the O-Cu-N angle in **4**-H_2O is supported by the electronic absorption spectrum of this complex obtained from TD DFT calculations shown in Figure S43. Lowest in energy in **4**-H_2O is a ligand $\rightarrow$ metal transition at 724 nm with $\pi_- \rightarrow x^2\text{-}y^2$ character that is close in energy to the corresponding transition in **1**-H_2O (754 nm). However, an equivalent of the lowest energy $\pi \rightarrow x^2\text{-}y^2$ (1,555 nm) transition in **1**-H_2O is absent in **4**-H_2O. The first $\pi_{Pyridine} \rightarrow x^2\text{-}y^2$ transition in **4**-H_2O only occurs in the UV at 313 nm and involves the excitation of an electron in a pyridine π orbital with vanishing amplitude at the coordinating nitrogen atom, implying

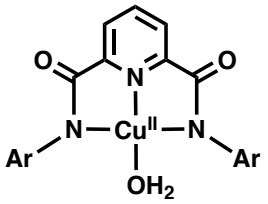

Figure S44. ChemDraw depiction of **4**-OH_2.

even higher energies for excitations from pyridine orbitals with a non-zero amplitude at this atom. Thus, although the central coordinating nitrogen in **1**-L and **4**-H_2O is formally =N–, the conjugation in the latter complex appears to have a major impact on the coordination geometry of copper.

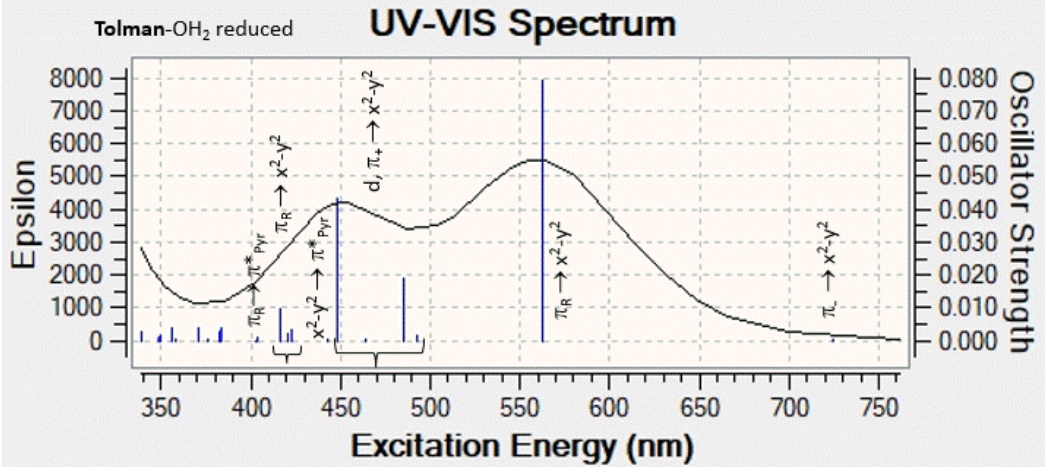

Figure S45. Electronic absorption spectrum for **4**-H_2O,[13] from B3LYP/TZVP TD-DFT calculations. The right-hand axis gives the scale for the oscillator strengths of the stick spectrum. The left-hand axis gives the scale of the absorptivity in M^{-1} cm^{-1} units. The spectrum (black solid curve) was constructed from the stick spectrum using a line width parameter of 0.2 eV. Transitions with wavelengths > 400 nm have been assigned based on analysis of the TD transitions. R labels the rings of the sidechains in the ligand R-N'-(O)C-Pyr-C(O)-N"-R.

9. Theoretical analysis of the zero-field splitting of the S = 1 ground state of 2-OH₂

As S = ½ systems have no ZFS, one might naively think that a coupled S = 1 state obtained by coupling two such systems, as in 1e-oxidized **2**-OH_2, has none either. However, this is not the case (D_{exp} = 3.5 cm^{-1}), due to anisotropic exchange. This interaction results from spin-orbit coupling (SOC) of the magnetic spin moment of the unpaired electron at Cu, where SOC is strongest, to the magnetic field generated by its orbital motion. The SOC makes the orbital state of the unpaired electron dependent on the magnetic quantum number of the electron. In fist-order perturbation theory one obtains the expressions

$$|x^2-y^2\,\alpha\rangle_a = \left(1+\left(\frac{\zeta}{2\Delta_{xz\rightarrow x^2-y^2}}\right)^2\right)^{-1/2}\left(|x^2-y^2\,\alpha\rangle + \frac{\frac{1}{2}i\zeta}{\Delta_{xz\rightarrow x^2-y^2}}|xz\,\alpha\rangle\right) \quad \text{(S8.1a)}$$

$$|x^2-y^2\,\beta\rangle_b = \left(1+\left(\frac{\zeta}{2\Delta_{xz\rightarrow x^2-y^2}}\right)^2\right)^{-1/2}\left(|x^2-y^2\,\beta\rangle - \frac{\frac{1}{2}i\zeta}{\Delta_{xz\rightarrow x^2-y^2}}|xz\,\beta\rangle\right) \quad \text{(S8.1b)}$$

for the SOC interaction between x^2-y^2 ground orbital and the xz excited orbital associated with Δg_y. The electronic spin states with $M_S = \pm 1/2$, denoted α and β in eqs S8.1a and S8.1b, are quantized along y: $\hat{s}_y\alpha = \frac{1}{2}\alpha$ and $\hat{s}_y\beta = -\frac{1}{2}\beta$. The admixure coefficients in eqs S8.1a and S8.1b are given by

$$\langle xz\,\alpha|\zeta\hat{\boldsymbol{l}}\cdot\hat{\boldsymbol{s}}|x^2-y^2\,\alpha\rangle = \zeta\langle xz|\hat{l}_y|x^2-y^2\rangle\,\langle\alpha|\hat{s}_y|\alpha\rangle = -\frac{1}{2}i\,\zeta \quad \text{(S8.2a)}$$

$$\langle xz\,\beta|\zeta\hat{\boldsymbol{l}}\cdot\hat{\boldsymbol{s}}|x^2-y^2\,\beta\rangle = \zeta\langle xz|\hat{l}_y|x^2-y^2\rangle\,\langle\beta|\hat{s}_y|\alpha\beta\rangle = +\frac{1}{2}i\,\zeta \quad \text{(S8.2b)}$$

The sign flip causes the M_S dependence of the orbital. Δg_y for the Cu site in eq S1.1b is related to the admixture coefficients as in

$$\Delta g_y = \frac{2\zeta}{\Delta_{xz\rightarrow x^2-y^2}} = 4\frac{\frac{1}{2}\zeta}{\Delta_{xz\rightarrow x^2-y^2}} \tag{S8.3}$$

and is four times the mixing coefficient divided by $i = \sqrt{-1}$. The g value for coupled $S = 1$ system is $\Delta g_y^c = \frac{1}{2}\Delta g_y$ and implies that the mixing coefficient, apart from factor i, is $\frac{1}{2}\Delta g_y^c$. Similarly, the mixing coefficient for $xy \rightarrow x^2$-y^2 is $\frac{1}{4}\Delta g_z^c$.

Without SOC the two spin-orbital states for the unpaired electron on Cu are simply the product of the same orbital state ($d = x^2$-y^2) and the $M_S = \pm 1/2$ spin states

$$d\,\alpha = |x^2 - y^2\,\alpha\rangle \tag{S8.4a}$$

$$d\,\beta = |x^2 - y^2\beta\rangle, \tag{S8.4b}$$

Combining the unpaired electron on Cu with the unpaired electron on the ligand (in orbital p) the M_S = 1 and 0 states for the 2-electron system without SOC are given by

$$|S = 1, M_S = 1\rangle = \frac{1}{\sqrt{2\left(1-\langle d|\pi\rangle^2\right)}}\big(d(1)\pi(2) - \pi(1)d(2)\big)\alpha(1)\alpha(2) = \frac{1}{\sqrt{1-\langle d|p\rangle^2}}\,\mathrm{A}\,\big(d(1)\alpha(1)\pi(2)\alpha(2)\big) \tag{S8.5a}$$

$$|S = 1, M_S = 0\rangle = \frac{1}{\sqrt{2\left(1-\langle d|\pi\rangle^2\right)}}\big(d(1)\pi(2) - \pi(1)d(2)\big)\frac{1}{\sqrt{2}}\big(\alpha(1)\beta(2) + \beta(1)\alpha(2)\big) =$$

$$\frac{1}{\sqrt{2\left(1-\langle d|\pi\rangle^2\right)}}\,\mathrm{A}\,\big(d(1)\alpha(1)\pi(2)\beta(2) + d(1)\beta(1)\pi(2)\alpha(2)\big) \tag{S8.5b}$$

$\mathrm{A} = \frac{1}{\sqrt{2}}\big(1 - (1,2)\big)$ is the Pauli antisymmetrization operator for a two-electron system.

When SOC is included, the 1-electron states in eqs S8.5a and S8.5b must be replaced by those given in eq S8.1a and S8.1b (SOC on the ligand is weak and has been ignored here), which can be written as products

$$d_a\,\alpha = |x^2 - y^2\,\alpha\rangle_a \tag{S8.6a}$$

$$d_b\,\beta = |x^2 - y^2\,\beta\rangle_b \tag{S8.6b}$$

in which the orbital factor depends on the spin. This dependence has been indicated by adding suffices a and b to the orbital part. The substitution yields the 2-electron states

$$|S = 1, M_S = 1\rangle = \frac{1}{\sqrt{1-\langle d|\pi\rangle^2}}\,\mathrm{A}\,\big(d_a(1)\alpha(1)\pi(2)\alpha(2)\big) \tag{S8.7a}$$

$$|S = 1, M_S = 0\rangle = \frac{1}{\sqrt{2\left(1-\langle d|\pi\rangle^2\right)}}\,\mathrm{A}\,\big(d_a(1)\alpha(1)\pi(2)\beta(2) + d_b(1)\beta(1)\pi(2)\alpha(2)\big) \tag{S8.7b}$$

Neglecting the squares of the overlap integral $\langle d|\pi\rangle^2$ relative to 1 in the normalization factors, the energies of these states simplify to

$$E(M_S = 1) = \langle S = 1, M_S = 1 | \hat{H}(1,2) | S = 1, M_S = 1 \rangle =$$

$$C - \frac{\frac{1}{4}\left(\Delta g_y^c\right)^2}{1+\frac{1}{4}\left(\Delta g_y^c\right)^2} \langle xz(1)\pi(2) | \hat{H}(1,2) | \pi(1)xz(2) \rangle \approx C + \frac{1}{4}\left(\Delta g_y^c\right)^2 \frac{J_{xz}}{2} \quad \text{(S8.8a)}$$

$$E(M_S = 0) = \langle S = 1, M_S = 0 | \hat{H}(1,2) | S = 1, M_S = 0 \rangle =$$

$$C + \frac{\frac{1}{4}\left(\Delta g_y^c\right)^2}{1+\frac{1}{4}\left(\Delta g_y^c\right)^2} \langle xz(1)\pi(2) | \hat{H}(1,2) | \pi(1)xz(2) \rangle \approx C - \frac{1}{4}\left(\Delta g_y^c\right)^2 \frac{J_{xz}}{2} \quad \text{(S8.8b)}$$

The brackets $\langle \quad \rangle$ represent the exchange term, which is obtained by taking spatial integral over the electronic variables 1 and 2 of the unpaired electrons. $\hat{H}(1,2)$ is the effective 2-electron Hamiltonian describing the two electrons in the potential of the nuclei and the other electrons in the molecule. *C* is a term which is independent of the magnetic quantum number M_S. The approximate equalities of eqs S8.8a and S8.8b assume that $\frac{1}{4}\left(\Delta g_y^c\right)^2 \ll 1$. Eqs S8.8a and S8.8b show that the energies of the magnetic substates $M_S = 1$ and 0 of the $S = 1$ manifold differ due to SOC. (The energy for $M_S = -1$ is equal to the energy for $M_S = +1$.) The energy splitting of the spin triplet state can be expressed by the zero-field splitting (ZFS) operator $D_y \hat{S}_y^{\,2}$, of which the ZFS parameter D_y is given eq S8.9.

$$D_y = E(M_S = 1) - E(M_S = 0) = \frac{1}{4}\left(\Delta g_y^c\right)^2 J_{xz} \quad \text{(S8.9)}$$

Relation between J_d ($d = xz$) and the factor in the $\langle \quad \rangle$ brackets in eqs S8.8a and S8.8b follows from the difference of the energies for the $S = 1$ and $S = 0$ states of the 2-electron system given in

$$|S = 1, M_S = 0\rangle = \frac{1}{\sqrt{2\left(1-\langle d|\pi\rangle^2\right)}}\left(d(1)\pi(2) - \pi(1)d(2)\right)\frac{1}{\sqrt{2}}\left(\alpha(1)\beta(2) + \beta(1)\alpha(2)\right) \quad \text{(S8.10a)}$$

$$|S = 0, M_S = 0\rangle = \frac{1}{\sqrt{2\left(1+\langle d|\pi\rangle^2\right)}}\left(d(1)\pi(2) + \pi(1)d(2)\right)\frac{1}{\sqrt{2}}\left(\alpha(1)\beta(2) - \beta(1)\alpha(2)\right) \quad \text{(S8.10b)}$$

Again, assuming that $\langle d|\pi\rangle^2 \ll 1$, these energies are given by

$$E(S = 1) \approx \langle d(1)\pi(2) | \hat{H}(1,2) | d(1)\pi(2) \rangle - \langle d(1)\pi(2) | \hat{H}(1,2) | \pi(1)d(2) \rangle \quad \text{(S8.11a)}$$

$$E(S = 0) \approx \langle d(1)\pi(2) | \hat{H}(1,2) | d(1)\pi(2) \rangle + \langle d(1)\pi(2) | \hat{H}(1,2) | \pi(1)d(2) \rangle \quad \text{(S8.11b)}$$

Using the convention $J_d \hat{\boldsymbol{S}}_{Cu} \cdot \hat{\boldsymbol{S}}_R$ for describing the exchange splitting between the two states, we obtain for $J_d = E(S = 1) - E(S = 0)$ the following expression:

$$J_d = -2\langle d(1)\pi(2) | \hat{H}(1,2) | \pi(1)d(2) \rangle \quad \text{(S8.12)}$$

The expression in eq S8.12 has been used to introduce the exchange parameter J_{xz} in eqs S8.8a and S8.8b. The above treatment of *J* follows the Heitler–London theory for the H_2 molecule with the 1*s* atomic orbitals of the hydrogen atoms in the molecule being replaced by the *d* and π orbitals carrying the unpaired electrons in the Cu–radical complex. The following two cases can be considered:

If $\langle d|\pi\rangle = 0$ the exchange term simplifies to the minus twice the positive 2-electron exchange integral,

$$J_d = -2\left\langle d(1)\pi(2)\left|\frac{1}{r_{12}}\right|\pi(1)d(2)\right\rangle < 0 \tag{S8.13a}$$

resulting in an $S = 1$ ground state.

If $\langle d|\pi\rangle \neq 0$ the exchange term contains also nuclear attraction integral terms, which dominate the 2e exchange integral by a large margin, making $J_d > 0$ and leading to an $S = 0$ ground state:

$$J_d = -2\langle d(1)\pi(2)|\hat{H}(1,2)|\pi(1)d(2)\rangle > 0 \tag{S8.13b}$$

This analysis forms the basis of the Kanamori–Goodenough rules for predicting the sign and magnitude of (super) exchange coupling constants in molecular complexes and solids.

Eq S8.9 implies that if J_d is antiferromagnetic ($J_d > 0$) then $D_y > 0$ and if J_d is ferromagnetic ($J_d < 0$) then $D_y < 0$. Thus, in the $J_d\hat{\boldsymbol{S}}_{Cu}\cdot\hat{\boldsymbol{S}}_R$ convention, the sign of D_y is the same as the sign of J_d. Obviously, since $\langle xz|\pi\rangle \neq 0$, $J_{x\tilde{z}} > 0$ and $D_y > 0$ ($x\tilde{z}$ orbital has a non-zero overlap integral with the $\pi_{\tilde{z}}$ type ligand orbital). There are also ZFS terms associated with Δg_x and Δg_z, respectively leading to the terms $D_x\hat{S}_x{}^2$ and $D_z\hat{S}_z{}^2$ in the ZFS operator,

$$\hat{H}_{ZFS} = D_x\hat{S}_x{}^2 + D_y\hat{S}_y{}^2 + D_z\hat{S}_z{}^2 - \frac{1}{3}(D_x + D_y + D_z)\hat{S}^2 \tag{S8.14}$$

with ZFS parameters given by

$$D_x = \frac{1}{4}(\Delta g_x^c)^2 J_{yz} < 0 \quad (\langle yz|\pi\rangle \approx 0) \tag{S8.15a}$$

$$D_y = \frac{1}{4}(\Delta g_y^c)^2 J_{xz} > 0 \quad (\langle xz|\pi\rangle \neq 0) \tag{S8.15b}$$

$$D_z = \frac{1}{16}(\Delta g_z^c)^2 J_{xy} < 0 \quad (\langle xy|\pi\rangle \approx 0) \tag{S8.15c}$$

Since the antiferromagnetic exchange coupling is anticipated to be stronger than the ferromagnetic exchange interactions, $J_{x\tilde{z}} >> |J_{xy}|, |J_{y\tilde{z}}|$, one expects that $D_y >> |D_x|, |D_z|$. In the limiting case that $D_x = D_z = 0$, eq S8.14 simplifies to

$$\hat{H}_{ZFS} = D\left[\hat{S}_y{}^2 - \frac{1}{3}S(S+1)\right] = D\left[\hat{S}_y{}^2 - \frac{2}{3}\right] \tag{S8.16}$$

with $D = D_y > 0$.

The model presented above explains the positive sign of D_{exp}. For $D_y = D_{exp} = 3.4$ cm^{-1} and $\Delta g_y^c = 0.03$ obtained by taking $\Delta g_y/2$ of the reduced water complex, eq S8.9 yields for $J_{x\tilde{z}}$ the value of 1.5 10^4 cm^{-1}. This value is extremely high, even for a direct exchange interaction. The value drops to 4 10^3 cm^{-1} by taking for Δg_y^c the value $\Delta g = 0.06$ inferred from EPR. While in the above model the magnetization axis is along y, the EPR analysis of the hyperfine splitting suggests that the magnetization axis bisects the y and $\tilde{z}$ axes. This property cannot be explained with SOC involving excitations to canonical 3*d* orbitals {*xy*, $x\tilde{z}$, $y\tilde{z}$, ...} but requires mixtures of those orbitals caused by low symmetry components in the ligand field. In this way, the principal axes of the *g* tensor rotate relative to those of the A^{SD} tensor, the latter being associated with the unpaired electron in the x^2-y^2 orbital and aligned with the {x, y, $\tilde{z}$} axes used in the definition of this orbital (Figure S34). The

distortion of the ibaps ligand plane and the contour plots of the orbitals suggest mixing of the xz and xy orbitals. The linear combinations

$$|\varphi_1\rangle = \sqrt{\frac{4}{5}}|xz\rangle - \sqrt{\frac{1}{5}}|xy\rangle \tag{S8.17a}$$

$$|\varphi_2\rangle = \sqrt{\frac{1}{5}}|xz\rangle + \sqrt{\frac{4}{5}}|xy\rangle \tag{S8.17b}$$

give the matrix elements for the angular momentum vector operator given in eqs S8.18a and S8.18b, respectively.

$$\langle\varphi_1|\hat{\boldsymbol{l}}|x^2-y^2\rangle = i\sqrt{\frac{8}{5}}\begin{pmatrix}0\\-1/\sqrt{2}\\-1/\sqrt{2}\end{pmatrix} \tag{S8.18a}$$

$$\langle\varphi_2|\hat{\boldsymbol{l}}|x^2-y^2\rangle = i\sqrt{\frac{8}{5}}\begin{pmatrix}0\\-1/\sqrt{2}\\+1/\sqrt{2}\end{pmatrix} \tag{S8.18b}$$

The vectors in eqs S8.18a and S8.18b bisect the y and z axes and are the principal axes for g tensor. Since $|\varphi_1\rangle$ and $|\varphi_2\rangle$ are close to $|xz\rangle$ and $|xy\rangle$, respectively, we have $J_{\varphi_1} \approx J_{xz} > 0$ and $J_{\varphi_2} \approx J_{xy} \approx 0$. If we refer to the direction defined by the vector in eq S8.18a as y' then we obtain for the zero-field splitting along this direction the expression

$$D_{y'} = \frac{5}{32}\left(\Delta g^c_{y'}\right)^2 J_{\varphi_1} \tag{S8.19}$$

From this expression we obtain J_{φ_1} = 6 10^3 cm^{-1}, using the values $D_{y'} = D_{\text{exp}}$ = 3.4 cm^{-1} and $\Delta g^c_{y'}$ = 0.06 inferred from parallel-mode EPR analysis. Although the value of J_{φ_1} is large compared to common ligand mediated "super" exchange couplings in binuclear transition-metal complexes, the direct nature of the coupling in 1e-oxidized **2**-OH_2 places it in the range of dative bonding energies.

10. Overlap integral of the N1 based p_z orbital and the tilted x^2-y^2 orbital of Cu.

In this section we evaluate the overlap integral between the N1-based p_z orbital and the tilted x^2-y^2 orbital of Cu. In this analysis, Cu is placed at the origin and N1 is located on the x axis at (R_{CuN1}, 0, 0). The tilted x^2-y^2 orbital at Cu is obtained by a rotation of this orbital over angle θ using the y axis as rotation axis and is given by x'^2-y^2, where $x' = \cos\theta\, x + \sin\theta\, z$. The normalized orbital, $|x'^2 - y^2\rangle$, can be expanded in the standard 3*d* orbitals as

$$|x'^2 - y^2\rangle = \cos\theta \sin\theta\, |xz\rangle + \tfrac{1}{2}\sqrt{3}\sin^2\theta\, |2z^2 - x^2 - y^2\rangle + \left(1 - \tfrac{1}{2}\sin^2\theta\right)|x^2 - y^2\rangle. \tag{S8.20}$$

Denoting the normalized p_z orbital at N1 as $|z\rangle$, the overlap integral of the tilted x^2-y^2 orbital and p_z is given by

$$\langle z|x'^2 - y^2\rangle = \cos\theta \sin\theta\, \langle z|xz\rangle + 0 + 0 \approx \theta\langle z|xz\rangle\,. \tag{S8.21}$$

The approximate equality sign is valid for small angles expressed in radians. Figure 12 shows that $\theta \approx (\pi - \angle$N1-Cu-X$)/2$, where X is the atom coordinated to Cu trans to N1.

Let us take the DFT structure of **2**-TMG as an example. This structure has distance R_{CuN1} = 2.0 Å and angle θ = 0.23 radians (13.4°). The overlap integral $\langle z|xz\rangle$ has been evaluated with G09 using the 2*p* and 3*d* orbitals of the basis set STO-3g and gives $\langle z|xz\rangle = 0.0064$ and consequently $\langle z|x'^2 - y^2\rangle$ = 0.00147.

As expected, the σ overlap integral $\langle x|x^2 - y^2\rangle$ = – 0.0175 is larger in magnitude than the π overlap integral $\langle z|xz\rangle$; furthermore, $\langle x|2z^2 - x^2 - y^2\rangle$ = 0.0101. With these values the tilting of the x^2-y^2 orbital changes in the σ overlap integral between p_x and x^2-y^2 and the change can be expressed as

$$\langle x|x'^2 - y^2\rangle - \langle x|x^2 - y^2\rangle = \tfrac{1}{2}\sqrt{3}\sin^2\theta\,\langle x|2z^2 - x^2 - y^2\rangle - \tfrac{1}{2}\sin^2\theta\;\langle x|x^2 - y^2\rangle \qquad \text{(S8.22)}$$

which gives the value of 0.00093, changing the negative σ overlap integral from –0.0175 to –0.0166. Thus, the lowering in the magnitude of the σ overlap integral (0.00093) is smaller than the increase in the π overlap integral (from 0 to 0.00147).

The overlap integrals between the atomic basis orbitals used here are smaller than between the orbital parts of the α and β SOMOs obtained from spin-unrestricted DFT calculations for the BS state. The overlap between the latter orbitals is larger due the p(N1)-d(Cu) mixing and leads to seizable energy splittings between the BS and ferromagnetic states (cf. Table 5).

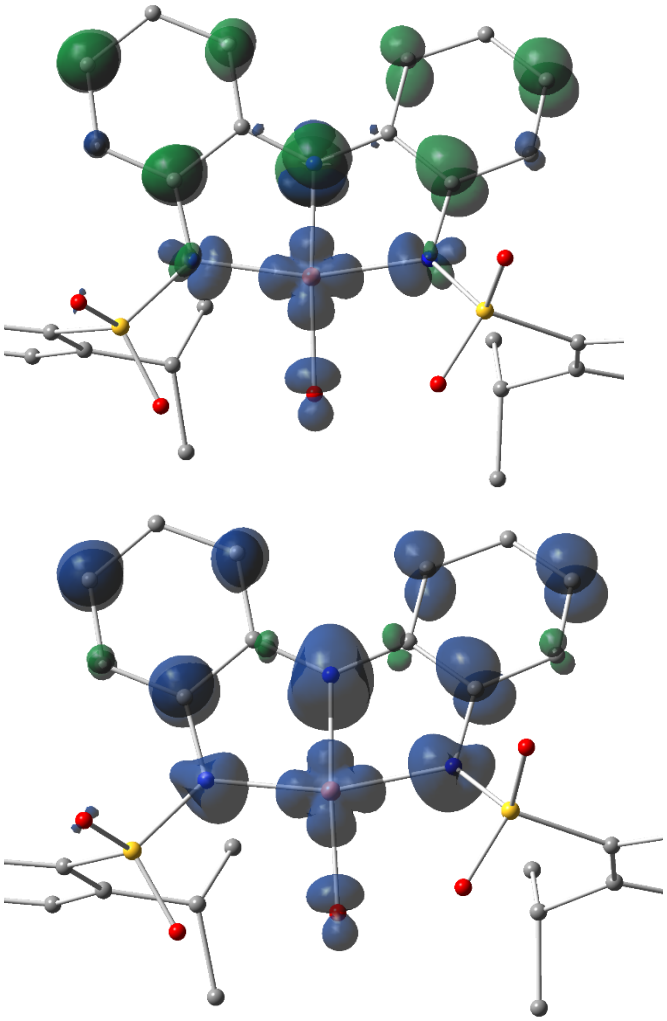

Figure S46. DFT (b3lyp/tzvp) spin density contours of **2**-OH_2 in the BS (top) and F (bottom) spin states using iso density value 0.005. H atoms are not shown for clarity.

References

1. Cook, S. A.; Bogart, J. A.; Levi, N.; Weitz, A. C.; Moore, C.; Rheingold, A. L.; Ziller, J. W.; Hendrich, M. P.; Borovik, A. S. Mononuclear complexes of a tridentate redox-active ligand with sulfonamido groups: Structure, properties, and reactivity. *Chem Sci* **2018**, *9*, 6540–6547.

2. Connelly, N. G.; Geiger, W. E. Chemical redox agents for organometallic chemistry. *Chem Rev* **1996**, *96*, 877–910.

3. Petasis, D. T.; Hendrich, M. P. Quantitative interpretation of multifrequency multimode EPR spectra of metal containing proteins, enzymes, and biomimetic complexes. *Methods Enzymol* **2015**, *563*, 171–208.

4. Kau, L.-S.; Spira-Solomon, D. J.; Penner-Hahn, J. E.; Hodgson, K. O.; Solomon, E. I. X-ray Absorption Edge Determination of the Oxidation State and Coordination Number of Copper:

Application to the Type 3 Site in *Rhus vernicifera* Laccase and Its Reaction with Oxygen. *J Am Chem Soc* **1987**, *109*, 6433–6442.

5. Dubois, J. L.; Mukherjee, P.; Collier, A. M.; Mayer, J. M.; Solomon, E. I.; Hedman, B.; Stack, T. D. P.; Hodgson, K. O. Cu K-Edge XAS Study of the $[Cu_2(\mu\text{-}O)_2]$ Core: Direct Experimental Evidence for the Presence of Cu(III). *J Am Chem Soc* **1997**, *199*, 8578–8579.

6. DuBois, J. L.; Mukherjee, P.; Stack, T. D. P.; Hedman, B.; Solomon, E. I.; Hodgson, K. O. A systematic K-edge X-ray absorption spectroscopic study of Cu(III) sites. *J Am Chem Soc* **2000**, *122*, 5775–5787.

7. Unjaroen, D.; Gericke, R.; Lovisari, M.; Nelis, D.; Mondal, P.; Pirovano, P.; Twamley, B.; Farquhar, E. R.; McDonald, A. R. High-Valent d^7 Ni^{III} versus d^8 Cu^{III} Oxidants in PCET. *Inorg Chem* **2019**, *58*, 16838–16848.

8. Sarangi, R.; Aboelella, N.; Fujisawa, K.; Tolman, W. B.; Hedman, B.; Hodgson, K. O.; Solomon, E. I. X-ray absorption edge spectroscopy and computational studies on $LCuO_2$ species: Superoxide-Cu^{II} versus peroxide-Cu^{III} bonding. *J Am Chem Soc* **2006**, *128*, 8286–8296.

9. Liu, Y.; Resch, S. G.; Klawitter, I.; Cutsail, G. E.; Demeshko, S.; Dechert, S.; Kühn, F. E.; DeBeer, S.; Meyer, F. An Adaptable N-Heterocyclic Carbene Macrocycle Hosting Copper in Three Oxidation States. *Angewandte Chemie* **2020**, *59*, 5696–5705.

10. Gautam, R.; Astashkin, A. V.; Chang, T. M.; Shearer, J.; Tomat, E. Interactions of Metal-Based and Ligand-Based Electronic Spins in Neutral Tripyrrindione π Dimers. *Inorg Chem* **2017**, *56*, 6755–6762.

11. Wu, T.; Macmillan, S. N.; Rajabimoghadam, K.; Siegler, M. A.; Lancaster, K. M.; Garcia-Bosch, I. Structure, Spectroscopy, and Reactivity of a Mononuclear Copper Hydroxide Complex in Three Molecular Oxidation States. *J Am Chem Soc* **2020**, *142*, 12265–12276.

12. Hitchman, M. A. Interpretation of Copper(II) Hyperfine Parameters. *Inorg Chem* **1985**, *24*, 4762–4765.

13. Donoghue, P. J.; Tehranchi, J.; Cramer, C. J.; Sarangi, R.; Solomon, E. I.; Tolman, W. B. Rapid C-H Bond Activation by a Monocopper(III)-Hydroxide Complex. *J Am Chem Soc* **2011**, *133*, 17602–17605.